Structure and Magnetic Properties of Intermetallic Rare-Earth-Transition-Metal Compounds: A Review

Lotfi Bessais

materials

MDPI

Review

Structure and Magnetic Properties of Intermetallic Rare-Earth-Transition-Metal Compounds: A Review

Lotfi Bessais

Department of Physics, University Paris Est Creteil, CNRS, ICMPE, 2 Rue Henri Dunant, F-94320 Thiais, France; bessais@icmpe.cnrs.fr; Tel.: +33-1-4978-1197

Abstract: This review discusses the properties of candidate compounds for semi-hard and hard magnetic applications. Their general formula is $R_{1-s}T_{5+2s}$ with R = rare earth, T = transition metal and $0 \leq s \leq 0.5$ and among them, the focus will be on the $ThMn_{12}$- and Th_2Zn_{17}-type structures. Not only will the influence of the structure on the magnetic properties be shown, but also the influence of various R and T elements on the intrinsic magnetic properties will be discussed (R = Y, Pr, Nd, Sm, Gd, ... and T = Fe, Co, Si, Al, Ga, Mo, Zr, Cr, Ti, V, ...). The influence of the microstructure on the extrinsic magnetic properties of these R–T based intermetallic nanomaterials, prepared by high energy ball milling followed by short annealing, will be also be shown. In addition, the electronic structure studied by DFT will be presented and compared to the results of experimental magnetic measurements as well as the hyperfine parameter determined by Mössbauer spectrometry.

Keywords: rare-earth-transition-metal intermetallics; mechanical alloying; hard magnetic materials; DFT; Mössbauer spectrometry

Citation: Bessais, L. Structure and Magnetic Properties of Intermetallic Rare-Earth-Transition-Metal Compounds: A Review. *Materials* **2022**, *15*, 201. https://doi.org/10.3390/ma15010201

Academic Editor: Hideki Hosoda

Received: 8 November 2021
Accepted: 14 December 2021
Published: 28 December 2021

1. Introduction

Rare-earth (R) and transition-metal (T, T = Co, Fe, Ni) based magnetic intermetallic compounds (IMC) have several key properties. These properties are divided into two categories: the intrinsic properties and the extrinsic properties. The intrinsic properties are the saturation magnetization (M_S), the Curie temperature (T_C), and the magnetocrystalline anisotropy (K_u). For the herein studied IMCs, these properties are determined by the crystallographic structure and the chemical composition, whereas the extrinsic properties are the coercivity H_C and the remanent magnetization M_R, which are mainly a function of the microstructure.

The IMCs' magnetic properties determine their potential application. Intermetallic compounds of the R–T type are formed with all rare-earths (R), except lanthanum for R_2Fe_{17}. These compounds are characterized by a rather low Curie temperature (T_C), which limits their field of application [1,2]. As generally observed for T-rich compounds, the low value of this temperature is attributed to T–T distances that are too short, particularly for T atoms that occupy the positions of the T–T dumbbells. For short distances between the T atoms, antiferromagnetic interactions occur instead of ferromagnetic interactions. As a result, considerable magnetic energy is stored, which leads to the lowering of the T_C values.

In addition, the magnetocaloric effect, around the Curie temperature, in some R–T intermetallic compounds is promising and has been actively studied in recent years [3–5].

The magnetocrystalline anisotropy of these compounds is governed by the combined effects of the anisotropy of the rare earth and transition metal atoms. In binary compounds, the rare earth anisotropy is very small at room temperature even though the rare earth sub-lattice has a uniaxial contribution to the anisotropy [6]. It is not sufficient to counteract the anisotropy of the transition metal sub-lattice at room temperature, which favors planar anisotropy.

In order to improve the magnetic properties, partial substitutions of the transition metal must be made and light elements, such as hydrogen, nitrogen or carbon, can be

inserted in interstitial positions of the unit cell. The increase in T_C and the change in anisotropy from planar to uniaxial opens the way for the use of these compounds in the field of permanent magnets or high-density magnetic recording. However, in addition to high-performance intrinsic properties, it is necessary to optimize the extrinsic properties (coercivity H_C, remanent magnetization M_R) by building a suitable microstructure corresponding to the envisaged applications. The microstructure must allow reaching the highest possible coercivity and remanent induction and a magnetization loop close to a rectangular one. The achievement of each of these objectives is facilitated by the existence of a granular microstructure [2,6–36].

The IMC can be magnetically hard, semi-hard, or soft. Hard intermetallics are characterized by their large hysteresis. They are used as permanent magnets. Semi-hard ones are used for high-density magnetic recording, while soft ones with a very small hysteresis are utilized in electromagnetic machines [37,38].

Figure 1 shows a simple approach to distinguish a hysteresis loop from a soft, semihard, or hard magnets, based on the coercivity H_C alone. A very wide loop has a high coercivity, while a narrow loop has a very low coercivity, and a semi-hard cycle has an intermediate coercivity. However, Coey has recently shown that we can define a coefficient, called hardness parameter κ, that determines more precisely the difference between these three categories of magnetic materials [38]. $\kappa = \sqrt{K_u / mu_0 M_S^2}$, where K_u is the anisotropy constant, M_S is the saturation magnetization, and μ_0 the vacuum permeability. For $\kappa < 0.1$ the magnet is soft, for $\kappa > 1$ the magnet is hard, and semihard magnets exhibit $\kappa < 1$.

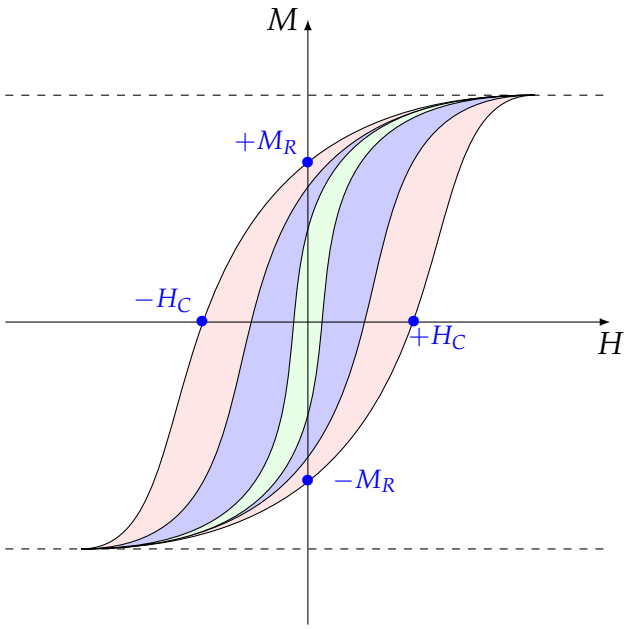

Figure 1. Hysteresis loops for hard (light red), semihard (light blue), and soft (light green) magnets. M the magnetization, H the applied magnetic field, M_R remanent magnetization, and H_C the coercivity.

Recently, Kovacs et al. [39] have clearly shown that one cannot expect a coercive field greater than 1 T in most rare-earth-free magnets. For this reason, the IMCs presented in this review are exclusively based on rare-earths and, more specifically, based on $CaCu_5$-type structure.

To enhance our understanding of *R*-*T* intermetallics for magnetic applications, we gather and discuss, in this review paper, the main achievements made in this field up to now. In particular, the influence of the structure and composition on the intrinsic magnetic properties will be discussed, as well as the effect of the synthesis methods on the extrinsic magnetic properties. A comparison between electronic properties determined by DFT and hyperfine parameters measured by Mössbauer spectrometry will also be shown.

2. Overview of Synthesis Methods for Improved Magnetic Properties

2.1. Methods for Synthesis of Intermetallic Compounds

Conventional techniques for the synthesis of intermetallic compounds consist of the arc or induction melting of pure elements with subsequent annealing. However, in material science, it is often observed that the synthesis method has a significant influence on the compound's properties. For the herein discussed compounds, it especially affects the microstructure but also the crystal structure, both of which influence the magnetic properties, as explained in the Introduction. Therefore, the choice of the synthesis method is a non-negligible key parameter.

In the example of *R*–*T* intermetallic compounds, it is often observed that conventional melting methods lead to polycrystalline alloys [40], whereas other techniques such as melt-spinning result in nanocrystalline alloys [41,42]. High-energy ball milling (HEBM) followed by annealing is another possible technique for the production of nanocrystalline alloys and it is well suited to the case of alloys based on rare-earth atoms, extremely volatile elements, because the reaction takes place below their melting temperature [43–48]. The annealing times of the powders can be very short, due to the their high reactivity of the nanometric crystallites obtained after HEBM. Moreover, this technique has the advantage of leading to large and homogeneous quantities of materials with reproducible characteristics. For these reasons, our group have chosen to produce *R*–*T*–*M* (*T* = Fe, Co, and *M* = Si, Al, Ga, Mo, Zr, Cr, Ti, V, ...) alloys by HEBM followed by annealing.

The powders of *R*, *T*, and *M*, are co-milled in a FRITSCH P7 planetary mill in hermetically sealed jars under a high purity argon atmosphere. The milling is performed in two steps: low energy grinding for half an hour followed by a HEBM for 5 h [44]. The obtained nanocrystalline powders are annealed for 30 min in sealed silica ampoules under a secondary vacuum. The annealing was performed at temperatures between 700 and 1100 °C depending on the desired phase, the out-of-equilibrium phase or the equilibrium one. As an example, for the equilibrium $R\bar{3}m$ Sm_2Fe_{17} phase the chosen temperature is 1050 °C, and to obtain the out-of-equilibrium $P6/mmm$ $SmFe_9$ phase, the annealing temperature is 700 °C.

2.2. Methods for Insertion of Light Elements in the Intermetallics

As mentioned in the Introduction, the insertion of light elements (i.e., H, N, C) in the crystal lattice is crucial for the optimization of the intrinsic magnetic properties.

Coey and Sun [8] introduced nitrogen into Sm_2Fe_{17} by heating ground powder in 1 bar of N_2 gas. After HEBM, S. V. Veselova et al. performed nitrogenation heat-treating the milled powder with a pressure equal to 40 atm at 450 °C for 24 h in the pure nitrogen atmosphere. Samples were nitrogenated with 2.4 nitrogen atoms per formula unit [49].

Phejar et al. have successfully prepared $La(Fe,Si)_{13}H_y$ hydrides by solid/gas reaction with a Sievert apparatus. The powder was introduced into a container, and then plugged to the hydrogenation apparatus. The sample was then submitted to a hydrogen pressure [44].

Unlike hydrides and nitrides, which were obtained exclusively by solid-gas reaction, carbides were elaborated by different methods:

(i) conventional fusion of appropriate quantities of samarium, iron, and gallium with a Fe-C pre-alloy under argon atmosphere with an excess of samarium [50,51];
(ii) a solid-gas reaction of the $Sm_2(Fe,M)_{17}$ alloy (obtained by conventional fusion) with a gaseous hydrocarbon [52,53];
(iii) high-energy ball milling from metallic elements, and reaction with a gaseous hydrocarbon [54].

Compared to nitrides and hydrides, carbides exhibit a greater thermal stability [55,56]. The insertion of the carbon in the elementary unit cell is achieved by a carbonation technique which involves a solid-solid type reaction [57–59]. The starting powders, $Sm_2(Fe,M)_{17}$, are finely ground, sieved (grain size less than 32 μm) and carefully mixed with the anthracene powder ($C_{14}H_{10}$) under high purity argon atmosphere. This technique consists in reacting the powder of $Sm_2Fe_{17-x}M_x$ compounds with anthracene, also in powder form,

in stoichiometric proportion. Each mixture is annealed, in a sealed silica ampoule under a secondary vacuum, for 24 h. The anthracene decomposes releasing hydrogen gas which is fixed by small pieces of magnesium previously placed in the ampoule and separated from the powder by silica wool. At the same time, the temperature was chosen so as not to modify the microstructure of the initial non-carbide alloys [44]. The carbon atoms, thus liberated, then diffuse in the compound according to the reaction:

$$7R - T + \frac{1}{2}C_{14}H_{10} + \frac{7}{2}Mg \longrightarrow 7R - T - C + \frac{5}{2}MgH_2.$$

3. Structure Analysis

A large number of rare earth-transition metal-based intermetallic alloys, whether equilibrium or non-equilibrium alloys are derived from the $CaCu_5$-type structure of space group $P6/mmm$, for example, $SmCo_5$ compound (Table 1). This structure is characterized by a crystallographic site ($1a$) for the rare earth atom at position (0,0,0) and two distinct sites for the transition metal atoms ($2c$) at position $(1/3, 2/3, 0)$ and ($3g$) at position $(1/2, 0, 1/2)$. The structure is shown in Figure 2. Over-stoichiometric cobalt equilibrium compounds of the RCo_5 phase have been studied previously. This results in a slight modification of the lattice due to the presence of cobalt atoms substituted for rare-earth atoms [60]. The general formula of these compounds becomes $R_{1-s}Co_{5+2s}$ [29,61,62], where a fraction s of the rare earth atoms is randomly replaced by pairs of Co atoms (dumbbell) parallel to the c axis. The deviation from the 1/5 stoichiometry strongly influences the magnetic properties of these compounds. For a higher stoichiometry deviation, ($s = 0.22$), the structure has been described as $TbCu_7$ [63–66].

Table 1. Atom Wyckoff positions, number of atoms in hexagonal $P6/mmm$ $R_{1-s}T_{5+2s}$ structure. $s = 0$, $s = 0.33$, and $s = 0.5$ correspond to $CaCu_5$, Th_2Zn_{17}, and $ThMn_{12}$ structure, respectively.

Atomic Position	**Occup.**	$s = 0$ **$CaCu_5$**	$s = 0.03$	$s = 0.33$ **2/17**	$s > 0.33$	$s = 0.5$ **1/12**
R($1a$) 0,0,0	$1 - s$	1	0.97	0.66	$1 - s$	0.5
T($2c$) $\frac{1}{3}, \frac{1}{2}, 0$	$2(1 - 3s)$	2	1.92	0	0	0
T($6l$) $x, 2x, 0$	$6s$	0	0.18	2	2	2
T($3g$) $\frac{1}{2}, 0, \frac{1}{2}$	3	3	3	3	3	3
T($2e$) $0, 0, z$	$2s$	0	0.06	0.66	$2s$	1

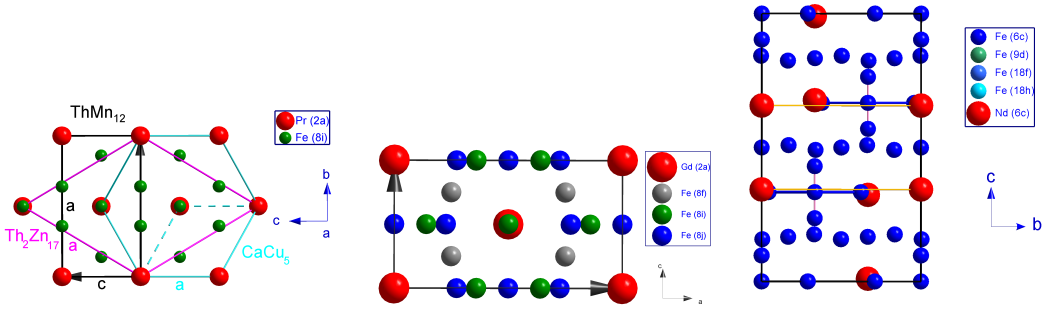

Figure 2. (**Left**) Schematic representation of the relationship between $CaCu_5$ (along [001] axis) Th_2Zn_{17} (along [001] axis) and $ThMn_{12}$ (along [010] axis) structures, (**Center**) illustration of atomic arrangements in $GdFe_{10}Cr_2$ crystal structure along [010] axis, and (**Right**) the rhombohedral $R\bar{3}m$ crystal structure of Nd_2Fe_{17} along [100] axis.

For specific values of s, the substitution becomes ordered and gives rise to derived crystal structures, among which the well-known equilibrium structures $ThMn_{12}$ ($s = 0.5$), Th_2Ni_{17}, and Th_2Zn_{17} ($s = 0.33$). For the latter, one R atom out of three is substituted in an ordered manner by an Fe–Fe pair. Figure 2 shows the relationship between $CaCu_5$, $ThMn_{12}$

and Th_2Zn_{17} structures. In this case, the precursor phase belongs to the $P6/mmm$ space group. For the Sm–Fe binary system, the $SmFe_5$ phase does not exist and the stoichiometry of the Sm_2Fe_{17} phase precursor has been described as $SmFe_9$ [23,29] and, very recently, using synchrotron resonant diffraction (SOLEIL), the stoichiometry of this phase has been definitely found as $SmFe_{8.5}$ [62] whereas it was considered in previous publications as $TbCu_7$ [63–72].

Moreover, D. B. de Mooij and K. H. J. Buschow have demonstrated [73] that the RFe_{12} binary compound cannot exist. Therefore, a third element M (M = Cr, Al, Ti, Mo, Si, W, or V) was required to stabilize this phase by forming a ternary $RFe_{12-x}M_x$.

The $TbCu_7$ designation (phase that can exist) attributed to the $SmFe_{12}$ [65,67,72] (phase that cannot exist [73]) adds an additional difficulty to understand the structure of these non-equilibrium phases.

A recent study [62] had the objective to find the structural relation between 2/17 and the non-equilibrium phase 1/9. On the other hand, this study removes the ambiguity that has often existed for the relationship between the hexagonal $TbCu_7$ phase and the hexagonal $P6/mmm$ phase precursor of the rhombohedral $R\bar{3}m$ phase.

3.1. Th_2Zn_{17}-Type Structure

The angular positions of the main diffraction peaks, $Sm_2Fe_{17-x}M_x$, show a crystallographic structure characteristic of the 2/17 phase of space group $R\bar{3}m$ (Figure 3). The refinement of the X-ray diffraction patterns (XRD) of $Sm_2Fe_{17-x}M_x$, is performed by the Rietveld method with the FULLPROF calculation code. This method also allows to determine the size of self-consistent diffraction domains. In the case of $Sm_2(Fe,M)_{17}$ compounds, the Rietveld refinement has been performed with the iron distributed on the four sites: 6*c*, 9*d*, 18*f*, 18*h* and the rare earth in site 6*c* (Table 2). These different crystallographic sites of the 2/17 rhombohedral phase are illustrated in Figure 2.

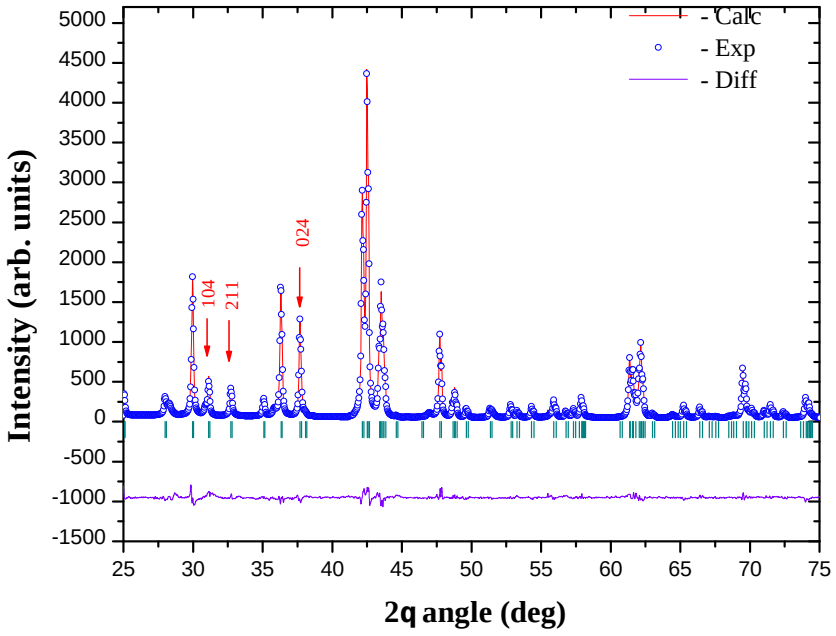

Figure 3. Rietveld refinement of XRD for nanocrystalline $Sm_2Fe_{16}Ga$ intermetallic.

Table 2. Atom and Wyckoff positions for the R_2Fe_{17} $R\bar{3}m$ rhombohedral structure.

Atom	Wyckoff Position
Sm 6*c*	(0,0,*z*)
Fe1 6*c*	(0,0,*z*)
Fe2 9*d*	$(\frac{1}{2},0,\frac{1}{2})$
Fe3 18*f*	(*x*,0,0)
Fe4 18*h*	(*x*,*x*,*z*)

As for the site occupied by *M* atoms, from the Mössbauer spectra explained later, we clearly exclude the occupation of the 6*c* sites (external shoulder on the positive velocity side, characteristic of the total occupation of the *c* site by iron). Site 9*d* being the smallest among the four sites 6*c*, 9*d*, 18*f* and 18*h*, was also excluded considering the high radius of *M* = Ga compared to Fe (r_{Fe} = 1.26 Å, r_{Ga} = 1.41 Å) [74]. In these conditions there remain two options: occupation of the site 18*h* or 18*f*. We clearly see a deterioration of this factor when gallium gradually occupies the 18*f* site. We therefore conclude that gallium is localized at 18*h*, which is in good agreement with the crystallographic results obtained by Teresiak et al. [24]. The structural results of XRD Rietveld refinement are presented for all compositions in Table 3.

Table 3. XRD analysis results obtained by Rietveld method on the $Sm_2Fe_{17-x}M_x$ (*M* = Si, Ga, Co, Zr, Cr, Mo) and (*x* = 0, 0.5, 1, 1.5, 2) alloys [25–30,62,75,76].

Alloy	a(Å)	c(Å)	$x(18f)$	$x(18h)$	$z(6c)$Sm	$z(6c)$Fe	$z1(8h)$	V(Å)^3	R_B	χ^2
Sm_2Fe_{17}	8.558	12.441	0.291	0.501	0.342	0.094	0.156	789	5.05	1.30
$Sm_2Fe_{16.5}Si_{0.5}$	8.547	12.437	0.291	0.501	0.341	0.095	0.156	787	4.62	2.10
$Sm_2Fe_{16}Si$	8.542	12.436	0.291	0.501	0.342	0.096	0.157	786	6.01	1.80
$Sm_2Fe_{15.5}Si_{1.5}$	8.527	12.428	0.291	0.501	0.342	0.095	0.157	782	4.40	2.40
$Sm_2Fe_{15}Si_2$	8.520	12.428	0.292	0.501	0.342	0.096	0.157	781	5.69	2.20
$Sm_2Fe_{16.5}Ga_{0.5}$	8.567	12.457	0.289	0.502	0.343	0.096	0.156	791	4.25	1.40
$Sm_2Fe_{16}Ga$	8.582	12.483	0.290	0.502	0.342	0.094	0.156	796	6.11	2.50
$Sm_2Fe_{15.5}Ga_{1.5}$	8.598	12.510	0.290	0.502	0.342	0.097	0.156	801	5.63	2.70
$Sm_2Fe_{15}Ga_2$	8.619	12.540	0.291	0.502	0.342	0.097	0.156	807	5.55	2.50
$Sm_2Fe_{16.5}Co_{0.5}$	8.550	12.450	0.289	0.501	0.343	0.096	0.156	788	4.56	1.61
$Sm_2Fe_{16}Co$	8.548	12.456	0.290	0.502	0.343	0.096	0.157	788	4.73	1.58
$Sm_2Fe_{15.5}Co_{1.5}$	8.545	12.463	0.291	0.501	0.343	0.096	0.156	788	4.05	1.40
$Sm_2Fe_{15}Co_2$	8.544	12.467	0.291	0.502	0.343	0.095	0.156	788	3.58	1.76
$Sm_2Fe_{16.5}Zr_{0.5}$	8.541	12.449	0.289	0.502	0.343	0.096	0.157	786	4.53	1.34
$Sm_2Fe_{16}Zr$	8.532	12.465	0.290	0.502	0.343	0.096	0.157	786	5.10	1.42
$Sm_2Fe_{15.5}Zr_{1.5}$	8.527	12.457	0.289	0.501	0.344	0.096	0.157	784	4.33	1.52
$Sm_2Fe_{16.5}Cr_{0.5}$	8.549	12.445	0.289	0.502	0.343	0.096	0.157	787	6.91	1.26
$Sm_2Fe_{16}Cr$	8.542	12.450	0.290	0.502	0.343	0.096	0.157	787	5.75	1.26
$Sm_2Fe_{15.5}Cr_{1.5}$	8.535	12.442	0.289	0.501	0.344	0.096	0.157	785	4.06	1.57
$Sm_2Fe_{15}Cr_2$	8.533	12.442	0.291	0.501	0.343	0.092	0.156	784	4.49	1.16
$Sm_2Fe_{16.42}Mo_{0.58}$	8.558	12.472	0.289	0.502	0.342	0.096	0.157	791	4.61	1.10

The unit cell parameters, *a* and *c*, as well as the volume increase with *x* in a linear way. This increase is due to the substitution of iron atoms by *M*, an element of greater atomic radius than iron. The size of the self-consistent diffraction domains is 60 nm for *x* = 0.5. Moreover, the Rietveld analysis allowed us to quantify the mass percentages of the phases present in the processed samples.

3.2. $ThMn_{12}$-Type Structure

RFe_{12} binary systems do not exist for any rare earth. Indeed, the atomic radius of iron is smaller than that of manganese in $ThMn_{12}$, in addition, according to the Pauling

classification of elements, iron has eight valence electrons against seven for manganese with a difference of electronegativity higher for iron compared to that with manganese. This induces a high electron density for the 8*i* site making the alloy unstable.

The reasons why this structure is unstable are therefore: interatomic distances that are too small and a very high electron density provided by iron. However, it is possible to stabilize the 1/12 structure by partially substituting iron with a third element of larger atomic radius; thus a 3*d* metal element or with a *p*-block element, this leads us to consider the chemical elements that are located to the left of iron in the periodic table.

Some authors report the obtaining of the $SmFe_{12}$ phase in thin films by non-equilibrium methods such as sputtering [77,78]. However, the obtained XRD pattern shows a simplified line system compared to that corresponding to the 1/12 phase. The explanation given by these authors is the strong texturing of the film along direction (002) obtained along the *c* axis. A refinement by the least square method was carried out, but adopting three different structures which all derive from the structure $CaCu_5$ structure; the $ThMn_{12}$, the Th_2Zn_{17} (2/17) and also the disordered hexagonal structure $TbCu_7$. The obtained lattice parameters are far from those related to the 2/17 phase. The observation of diffraction patterns does not clarify the nature of the phase, which remains ambiguous, since no indexation is provided but only a suggestion that the phase 1/12 is the closest.

The 1/12 phase could be stabilized by several elements such as Ti [25,79–84], Si [80], Mo [79,80,85], W [73,79,80], Cr [79,80,86], V [79,83,87], Al [80]. The solubility and the range of existence of the $RFe_{12-x}M_x$ phase vary from one substituent to another. The interest of these phases lies in their Curie temperature which is relatively high compared to that of the 2/17 alloys. It has been shown [88], by ab-initio calculation, that the solubility of Mo is higher than that of Ti, which is in agreement with experiment [89]. When the M (M = Cr, V, Ti, Mo) atoms substitute the Fe atoms in the 8*i* site, the cohesive energy decreases in a more significant way than when the M atoms go into the Fe 8*j* or 8*f* sites. Therefore, the substituents M preferentially occupy the 8*i* site. The rare earth occupies the 2*a* (0,0,0) site. As for the elements Fe and M, they are distributed on three crystallographic sites: 8*i* (0.36,0,0), 8*j* (0.27,$\frac{1}{2}$,0) and 8*f* ($\frac{1}{4}$, $\frac{1}{4}$, $\frac{1}{4}$) see Figure 2. The atomic positions and the symmetry of the different sites are presented in the Table 4.

Table 4. Atom and Wyckoff positions for the $RFe_{11}Ti$ $I4/mmm$ tetragonal structure.

Atom	Symmetry	Wyckoff Position
R 2*a*	$4/mmm$	(0,0,0)
Fe1 8*f*	$2/m$	($\frac{1}{4}$,$\frac{1}{4}$,$\frac{1}{4}$)
Fe2 8*i*	$m2m$	(x,0,0)
Fe3 8*j*	$m2m$	(x,$\frac{1}{2}$,0)

The works relating to 1:12 phases based on praseodymium and 3*d* transition metals (Fe, Ti, Mo, V) [90,91] report on the difficulties related to their elaboration. Indeed, the nature of the phases obtained and their relative abundances in the sample are closely linked to the annealing temperature. Thus the $PrFe_{11}Ti$ phase ($I4/mmm$) is obtained mainly in a very small range of annealing temperatures (80 K) between 1303 K and 1383 K. Below 1173 K the majority phase is the 2:17 phase. On the other hand, above 1383 K a peritectic decomposition leads to the precipitation of $\alpha-$(Fe,Ti) which considerably reduces the abundance of the 1:12 phase.

The $ThMn_{12}$ structure derives from the $CaCu_5$ structure and can be schematized by the relation:

$$2\,RT_5 \;-\; R \;+2\,T \;=\; RT_{12}.$$

Half of the rare earth atoms of the 1/5 structure are replaced by a *T*–*T* pair at position 8*i* in the 1/12 structure. The unit cell parameters of the two related structures are described by the following expressions (Figure 2):

$$a(1/12) = b(1/12) = \frac{2}{3}c(1/12) \quad ; \quad a(1/5) = c(1/12).$$

The refinement of the XRD patterns allowed us to derive the size of the self-consistent diffraction domains and to quantify the mass fractions of the minority phases present. Structural study of the unit cell parameters were systematically measured with an Si standard. The refinement of the diffraction patterns was performed by considering the iron atoms statistically distributed on the different sites 8*i*, 8*j* and 8*f* and considering the substituent M atoms on the site 8*i*. The unit cell parameters are given in Table 5. Note also that the ratio c/a is not far from the theoretical value $1/\sqrt{3}$ of the tetragonal structure.

Table 5. XRD analysis results obtained by Rietveld method on the $RFe_{12-x}M_x$ (M = Si, Ti, Cr, V, Cr, Mo) and (x = 0, 0.5, 1, 1.5, 2) alloys [25–30,62,75,76,82,84].

Alloy	a(Å)	c(Å)	Ref.
$YFe_{11}Ti$	8.503(3)	4.789(4)	[84]
$SmFe_{11}Ti$	8.555(3)	4.794(3)	[25]
$YFe_{10.5}Mo_{1.5}$	8.527(2)	4.784(2)	[92]
$CeFe_{10.5}Mo_{1.5}$	8.535(1)	4.769(2)	[92]
$PrFe_{10.5}Mo_{1.5}$	8.600(2)	4.785(3)	[92]
$NdFe_{10.5}Mo_{1.5}$	8.584(1)	4.780(2)	[92]
$SmFe_{11}Mo$	8.565(2)	4.786(2)	[29]
$GdFe_{10.5}Mo_{1.5}$	8.553(2)	4.795(1)	[92]
$TbFe_{10.5}Mo_{1.5}$	8.562(2)	4.782(1)	[92]
$DyFe_{10.5}Mo_{1.5}$	8.523(1)	4.782(1)	[92]
$HoFe_{10.5}Mo_{1.5}$	8.518(3)	4.786(3)	[92]
$ErFe_{10.5}Mo_{1.5}$	8.515(2)	4.783(1)	[92]
$LuFe_{10.5}Mo_{1.5}$	8.483(3)	4.770(2)	[92]
$SmFe_{10}V_2$	8.528(6)	4.770(3)	[83]
$PrFe_{11}Ti$	8.594(2)	4.789(2)	[84]
$NdFe_{11}Ti$	8.579(3)	4.795(2)	[83]
$GdFe_{11}Ti$	8.533(3)	4.789(3)	[93]
$GdFe_{10}Cr_2$	8.480(6)	4.755(3)	[86]

E. Tomey et al. [92] found that, for the $RFe_{10.5}Mo_{1.5}$ series of compounds, where R goes from Pr to Lu, the lattice parameter a decreases as a function of R while the c parameter remains quasi-constant. The parameter a is governed by the atomic radius of the rare-earth.

4. Intrinsic Magnetic Properties

In this section, we do not present exclusively the IMCs prepared by HEBM, since the intrinsic properties are independent of the microstructure, and therefore of the synthesis method.

4.1. Curie Temperature

For nanocrystalline intermetallics, the Curie temperature, which represents the ferro-paramagnetic transition, must be relatively high for a permanent magnet or for high density magnetic recording applications. Generally, there are two strategies to increase T_C, either substituting the iron by another metal, or inserting a light element (C, H, N . . .) in the unit cell of the intermetallic compound.

Figure 4 (Left) shows the dependence of Curie temperature on the rare-earth atom for the R_2Fe_{17} structure. This behavior is due mainly to the variation of the de Gennes factors of the different rare-earth atoms. The Curie temperature variation for the different rare-earth atom resembles that of the magnetic hyperfine field as we will see later.

The Curie temperatures of $Sm_2Fe_{17-x}M_x$ compounds were measured on sealed ampoule samples under the secondary vacuum with an applied field of 1000 Oe. T_C was determined by the minima in dM/dT curves, derived from the magnetization measurements.

In R_2Fe_{17} intermetallic compounds, the Curie temperature (T_C) is low, around room temperature (418 K for Sm_2Fe_{17}) [23]. This is mainly due to the short Fe–Fe inter-atomic distances of the dumbbells (6*c* for the $R\bar{3}m$ Sm_2Fe_{17} structure [94] and 2*e* for $P6/mmm$ $SmFe_{8.5}$ [62]), where the Fe atoms are anti-ferromagnetically coupled. This distance attached to the dumbbell sites, less than 2.45 Å, leads to negative Fe–Fe interactions [7,95] (Figure 4 (Right)).

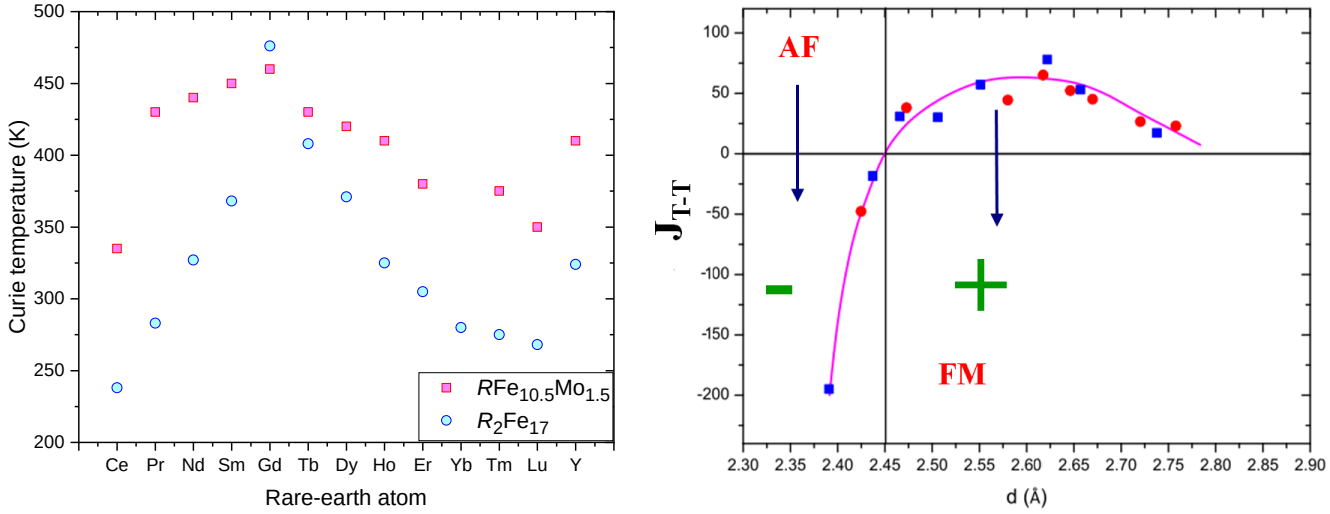

Figure 4. (**Left**) Curie temperatures for different rare-earth atoms, for R_2Fe_{17} and $RFe_{10.5}Mo_{1.5}$ [28,30,75,96–98]. (**Right**) Exchange interaction $J_{T\text{-}T}$ vs. distances between transition metal atoms (T–T) for Sm_2T_{17}. For interatomic T–T distances less than 2.45 Å the exchange interaction ($J_{T\text{-}T}$) is negative, while $J_{T\text{-}T}$ is positive in the opposite case [94].

With the substitution of M atoms in the compounds $Sm_2Fe_{17-x}M_x$, the Curie temperature increases monotonically with x, then T_C decreases (Figure 5, Table 6).

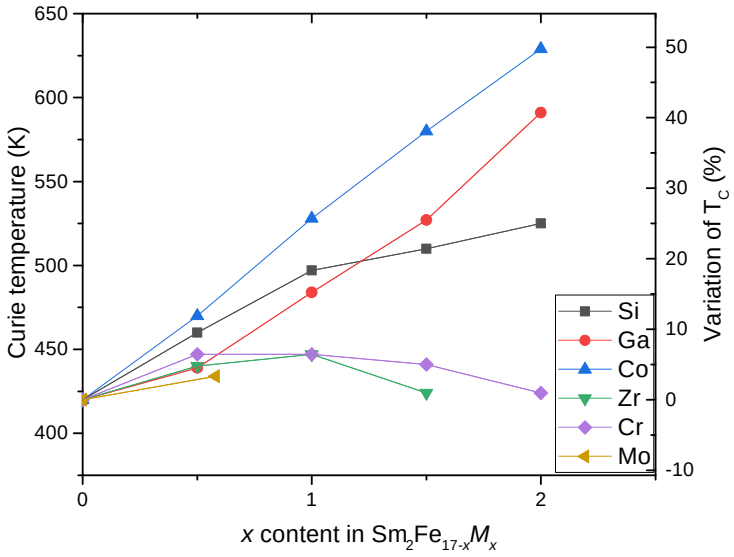

Figure 5. Curie temperature T_C and variation $\Delta T_C/T_C$ of $Sm_2Fe_{17-x}M_x$ for M = Si, Ga, Co, Zr, Cr, Mo [28,30,75,96–98].

Table 6. Curie temperature of $Sm_2Fe_{17-x}M_x$ (M = Si, Ga, Co, Zr, Cr, Mo) and (x = 0, 0.5, 1, 1.5, 2) alloys.

Alloy	T_C (K)	References
Sm_2Fe_{17}	420	[97]
$Sm_2Fe_{16.5}Si_{0.5}$	460	[96]
$Sm_2Fe_{16}Si$	497	
$Sm_2Fe_{15.5}Si_{1.5}$	510	
$Sm_2Fe_{15}Si_2$	525	
$Sm_2Fe_{16.5}Ga_{0.5}$	439	[97]
$Sm_2Fe_{16}Ga$	484	
$Sm_2Fe_{15.5}Ga_{1.5}$	527	
$Sm_2Fe_{15}Ga_2$	591	
$Sm_2Fe_{15}Ga_3$	596	
$Sm_2Fe_{16.5}Co_{0.5}$	696	[28]
$Sm_2Fe_{16}Co$	707	
$Sm_2Fe_{15.5}Co_{1.5}$	717	
$Sm_2Fe_{15}Co_2$	732	
$Sm_2Fe_{16.5}Zr_{0.5}$	440	[76]
$Sm_2Fe_{16}Zr$	447	
$Sm_2Fe_{15.5}Zr_{1.5}$	424	
$Sm_2Fe_{16.5}Cr_{0.5}$	447	[75]
$Sm_2Fe_{16}Cr$	447	
$Sm_2Fe_{15.5}Cr_{1.5}$	441	
$Sm_2Fe_{15}Cr_2$	424	
$Sm_2Fe_{16.42}Mo_{0.58}$	434	[29]

The Curie temperature, for rare-earth-transition-metal compounds, is governed, in general, by three types of interactions:

- $3d$–$3d$ (J_{FeFe}) exchange interaction between the magnetic moments of the transition-metal atom sublattice;
- $4f$–$4f$ (J_{RR}) exchange between $4f$–$4f$ magnetic moments of Sm lattice atoms;
- $3d$–$4f$ (J_{RFe}) exchange between the two $3d$–$4f$ sublattices.

The $4f$–$4f$ exchange interaction can be neglected since it is the weakest of the three interactions. We can consider that the only contribution to the Curie temperature is due to the interaction between the magnetic moments of the iron sublattice ($3d$–$3d$), if in addition we can also neglect the interactions between the two sublattices ($3d$–$4f$) by considering an R-Fe system with non-magnetic R atom.

In compounds with a rhombohedral structure, the Fe($6c$)–Fe($6c$) interactions are negative. This is also the case for Fe($9d$)–Fe($18f$) (weakly negative), while the other Fe–Fe interactions are positive. It was found, for the $Sm_2Fe_{17-x}M_x$ compounds, that the J_{FeFe} interaction augments up to x = 3. It has also been reported that the coupling constant of the J_{SmFe} sublattices is very small compared to that of J_{FeFe} and it is nearly unrelated to the M content. This shows that the Curie temperature is mostly monitored by J_{FeFe}. The combination of the two effects, magnetovolume and electronic, can explain the evolution of the Curie temperature. The substitution of non-magnetic elements, such as silicon and aluminum on iron sites in R_2Fe_{17} compounds, gives a variation of T_C similar to M substitution (Figure 5).

4.2. Hyperfine Parameters

Mössbauer spectrometry is a particularly recommended technique for samarium-based alloys with an absorption coefficient such that neutron diffraction studies remain very difficult to perform. It allows to confirm the structural results and to determine the hyperfine parameters.

The Mössbauer spectra analysis is based on an adapted and precise simulation method which takes into account the isomer shift (δ). This quantity, which accounts for the density of s electrons at the nucleus, is an essential data to understand the effect of the insertion of the light element.

One may be tempted to use a large number of parameters to get a satisfactory simulation. However, the selected solution for the refinement of the Mössbauer spectra must match a physical model supported by several experimental techniques or it could be based on relevant theoretical approaches. The credibility of the suggested model for the fitting of the spectra must be proved by the uniform evolution of the set of hyperfine parameters with a line width slightly higher than the value of 0.25 mm/s, corresponding to the experimental width of the reference α–Fe (Figures 6–8).

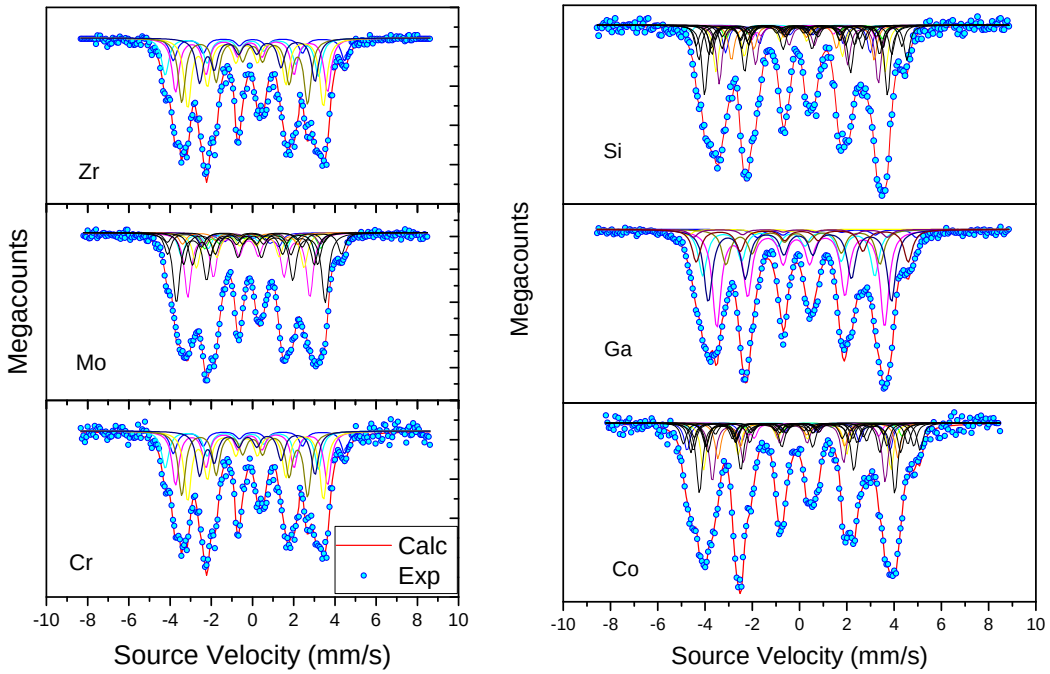

Figure 6. The room temperature Mössbauer spectra of $Sm_2Fe_{16}M$ (M = Zr, Mo, Cr, Si, Ga, Co) [28,30,75,96–98].

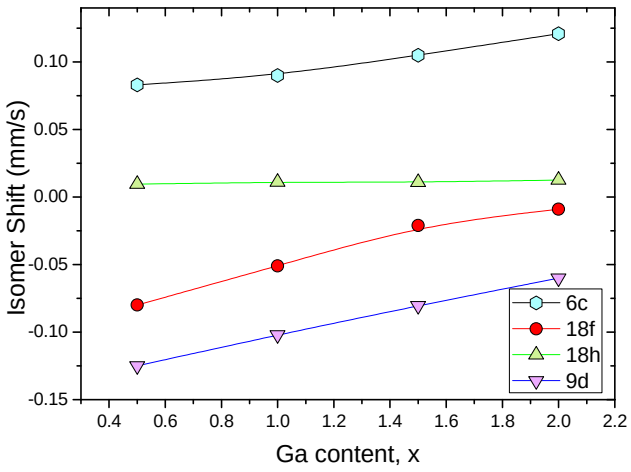

Figure 7. Isomer shift evolution vs substituted Ga atom composition for $Sm_2Fe_{17-x}Ga_x$.

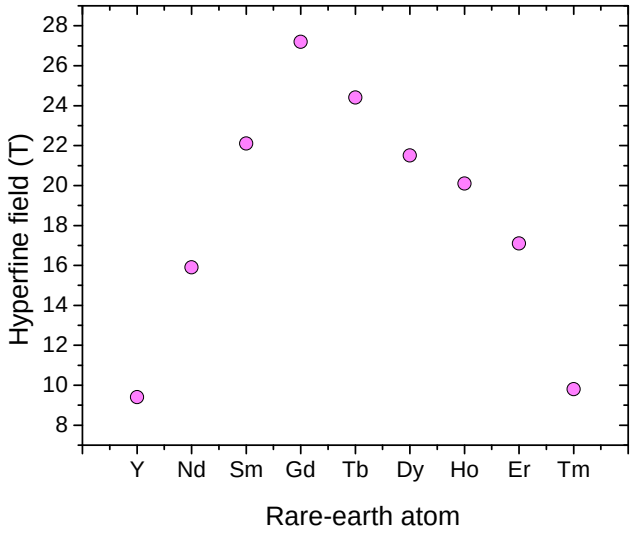

Figure 8. Hyperfine field for different R_2Fe_{17} [38,42,99–104].

In addition, the line intensities of the sextuplets were considered in the ratio 3:2:1:1:2:3, assuming a randomly oriented powder, in good agreement with the absence of texture observed on the XRD patterns. A line-width equal to 0.27 mm/s was generally used for each individual sextuplet of the rhombohedral $R\bar{3}m$ Th_2Zn_{17}- and the tetragonal $I4/mmm$ $ThMn_{12}$-type structure. Furthermore, we supposed that the Lamb–Mössbauer absorption factor is the same for all non-equivalent crystallographic sites.

The good resolution of the spectra combined with the crystallographic studies allows a detailed analysis. The refinement of the spectra is then based, on the one hand, on a counting approach of the various magnetic subsites, and on the other hand, on the attribution to these sites of the hyperfine parameters resulting from a good simulation of the spectra for a defined and fixed number of observable sites. Moreover, the evolution of the hyperfine parameters must be coherent and monotonous as a function of the substituted atom rate (Table 7).

Table 7. Hyperfine parameters of R_2Fe_{17-x}.

	$\mu_0 H_{HF}(T)$	Ref
Y_2Fe_{17}	9.4(2)	[99]
Nd_2Fe_{17}	15.9(1)	[100]
Sm_2Fe_{17}	22.1(2)	[38]
Gd_2Fe_{17}	27.2(2)	[101]
Tb_2Fe_{17}	24.4(1)	[102]
Dy_2Fe_{17}	21.5(4)	[42]
Ho_2Fe_{17}	20.1(2)	[99]
Tm_2Fe_{17}	17.1(1)	[103]
Er_2Fe_{17}	9.8(1)	[104]

The most rigorous method to assign the different sextuplets to the non-equivalent crystallographic sites (6*c*, 9*d*, 18*f* and 18*h* for Th_2Zn_{17} phase, and 8*i*, 8*j*, 18*f* and 18*h* for $ThMn_{12}$ phase) takes into account the hyperfine fields, δ and the Wigner–Seitz cell volumes (WSC). The correlation between the Wigner-Seitz cell volumes and the isomer shift has been established [21,25,82,84,86]. The larger the isomer shift, the larger WSC volume. In addition, the larger the number of iron neighbors of a resonant iron atom, the larger the hyperfine field.

The general approach used for the refinement of the spectra of the different structures will take into account, on the one hand, the correlation between the WSC volumes and δ, and on the other hand, the exact calculation of the abundances of the different sub-sites by means of a binomial distribution law of the substituted atoms.

Mössbauer spectra of the $Sm_2(Fe,M)_{17}$ samples (M = Ga, Zr, Si, Mo, Cr and Co) recorded at room temperature are shown in Figure 6. These spectra are very complex and magnetically ordered. They result from the convolution of many subspectra; this is due to the existence of the four inequivalent Fe sites, disturbed by the substitution of Fe by the M atom at 18h position. The isomer shift of $6c, 18f, 9d$ sites slightly increases with the rate of M atoms, while that of the site 18h remains constant within the limits of the experimental precision. This particular behavior of the $\delta\{18h\}$ confirms the position of the M atom in this specific site.

It should be noted that δ resulting from the sequence of Wigner-Seitz cell calculated volumes: $\delta\{6c\} > \delta\{18h\} > \delta\{18f\} > \delta\{9d\}$ reflect well the perturbations brought by the substitution of iron by the M atom, in perfect agreement with the nature of the different environments. Moreover, the evolution of the hyperfine magnetic fields brings an additional argument to the approach we have led.

Figure 8 shows the dependence of hyperfine field (H_{HF}) on the rare-earth atom for R_2Fe_{17} structure (Table 7). The change of the H_{HF} with different rare earth atoms resembles that of the Curie temperature (Figure 4).

The refinement of the hyperfine fields is derived from the analysis of δ since the inequivalent iron site is defined by a set of hyperfine parameters H_{hf} and δ. It follows that $H_{hf}\{6c\} > H_{hf}\{9d\} > H_{hf}\{18f\} > H_{hf}\{18h\}$. Moreover, H_{hf} strength of a given atom depends on the number of Fe neighbors: the larger the number of Fe neighbors, the higher H_{hf}. The hyperfine field analysis is in perfect agreement with this relationship, site 6c with 13 iron neighbors is by far the largest. Sites 9d and 18f with 10 iron neighbors show average field values, while site 18h with 9 neighbors is the smallest (Figure 9).

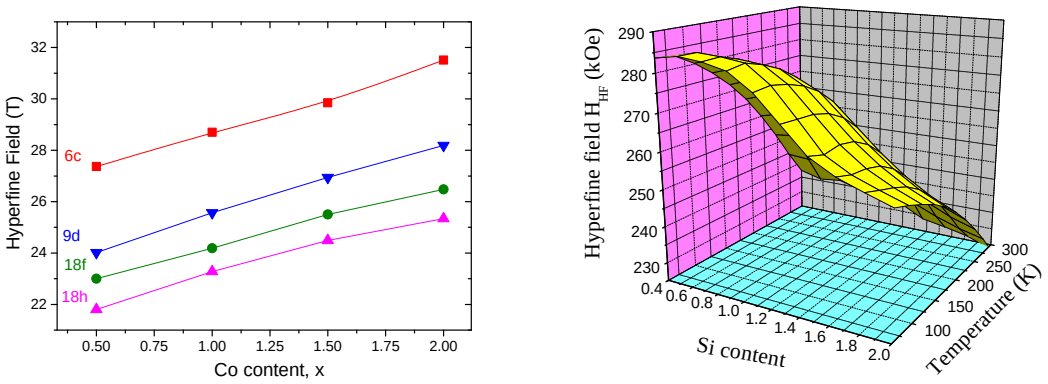

Figure 9. (**Left**) Hyperfine field evolution vs substituted Co atom composition for $Sm_2Fe_{17-x}Co_x$. (**Right**) The dependence of hyperfine field on Si content and temperature for $Sm_2Fe_{17-x}Si_x$.

Concerning the tetragonal $I4/mmm$ $ThMn_{12}$-type structure several studies were devoted to $RFe_{11}Ti$ (R = Y, Pr, Nd, Sm, Gd) intermetallics [25,84,86,105–107]. The refined hyperfine field (H_{HF}), isomer shift (δ), and quadrupole interaction (2ε) for the studied intermetallics are presented in Table 8. For these compounds the following sequence for the hyperfine field was found $H_{HF}\{8i\} > H_{HF}\{8j\} > H_{HF}\{8f\}$, which is coherent with the number of nearest iron neighbors for each inequivalent crystallographic site.

Table 8. Room temperature Mössbauer hyperfine parameters for $RFe_{12-x}M_x$: Hyperfine field (H_{HF}), isomer shift (δ) and quadrupole interaction (2ε). $\langle HF \rangle$ denotes the average of the hyperfine parameters.

	Fe{8*i*}	**Fe{8*j*}**	**Fe{8*f*}**	**⟨HF⟩**	**Ref.**
$YFe_{11}Ti$					[84]
$\mu_0 H_{HF}$(T)	26.8	22.7	20.1	23.2	
δ (mm/s)	−0.09	−0.12	−0.17	−0.13	
2ε (mm/s)	0.08	0.07	0.04	0.06	
$PrFe_{11}Ti$					[84]
$\mu_0 H_{HF}$(T)	27.1	23.8	21.8	24.2	
δ (mm/s)	−0.08	−0.10	−0.12	−0.09	
2ε (mm/s)	0.09	0.09	0.04	0.08	
$NdFe_{11}Ti$					[105]
$\mu_0 H_{HF}$(T)	32.6	29.6	25.2	28.1	
δ (mm/s)	0.01	−0.02	−0.15	−0.09	
2ε (mm/s)	0.03	0.10	0.02	0.08	
$SmFe_{11}Ti$					[25]
$\mu_0 H_{HF}$(T)	27.2	23.5	25.8	28.1	
δ (mm/s)	0.01	−0.02	−0.15	−0.09	
2ε (mm/s)	0.03	0.10	0.02	0.08	
$GdFe_{11}Ti$					[86]
$\mu_0 H_{HF}$(T)	26.9	25.1	23.9	25.1	
δ (mm/s)	−0.06	−0.11	−0.13	0.14	
2ε (mm/s)	0.05	0.04	0.04	0.04	

4.3. DFT Calculation

The DFT calculation is very useful, not only to calculate the formation energy of intermetallic compounds, but also to determine the theoretical hyperfine field and finally to calculate the total and individual partial magnetic moment per crystallographic site. The objective of the theoretical calculations is to compare the formation energies of the compounds in order to be able to evaluate their stability, and to compare the theoretical and experimental magnetic moments deduced from the Mössbauer spectrometry.

Harashima et al. utilizing first-principal calculations have demonstrated that for any rare-earth R atom [108,109] the binary rhombohedral R_2Fe_{17} with Th_2Zn_{17}-type structure is more stable than the tetragonal RFe_{12} with $ThMn_{12}$-type structure. However, if the rare-earth R atom (R = Nd or Sm) is partially replaced by Zr, Y or Dy, the difference between the formation energies of 2/17 and 1/12 is lowered.

The magnetic moments for the rhombohedral Sm_2Fe_{17} compound was calculated by Yamashita et al. [110] using ab initio approach. The results of these calculations give the following values of magnetic moments for the four inequivalent crystallographic sites: $\mu_{6c} = 2.67\ \mu_B$, $\mu_{18f} = 2.49\ \mu_B$, $\mu_{18h} = 2.39\ \mu_B$, and $\mu_{9d} = 2.21\ \mu_B$. These values are consistent with those found by Ogura et al. using first-principles electronic structure calculations [111] (Figure 10).

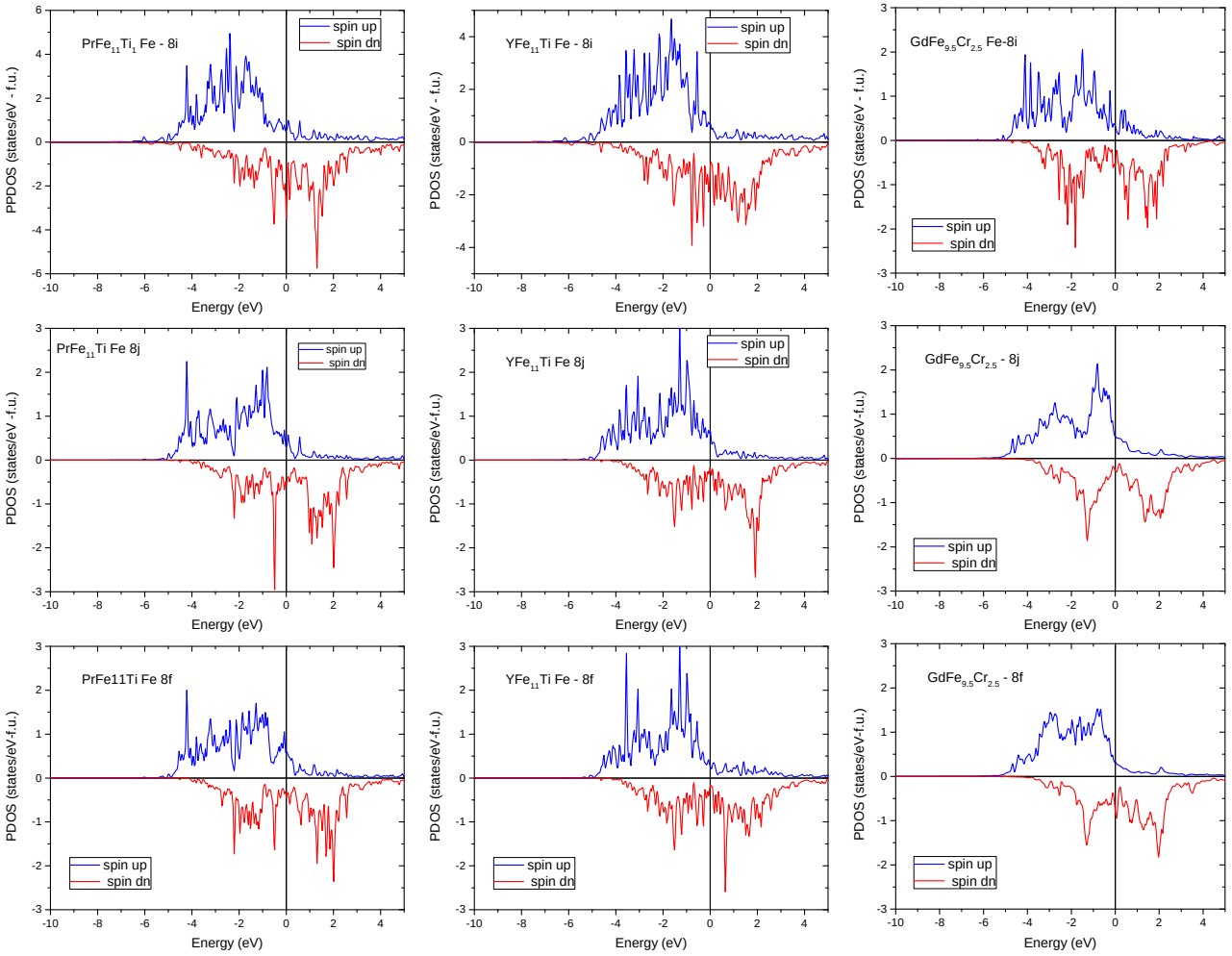

Figure 10. Partial density of states for Fe-8*i*, Fe 8*j* and Fe-8*f* calculated for (**left**) $PrFe_{11}Ti$, (**middle**) $YFe_{11}Ti$ and (**right**) $GdFe_{9.5}Cr_{2.5}$. The origin of the energy is located at Fermi energy (black vertical line).

For the tetragonal $GdFe_{12-x}Cr_x$ compound, the DFT calculation allows, among other things, to determine the site of Cr occupation in the $I4/mmm$ space group. The total energy of $GdFe_{12-x}Cr_x$ has been calculated for the three possible substitution Cr sites. This calculation showed that the lowest total energy is consistent with the substitution of iron with chromium in the 8*i* site (Table 9), indicating that Cr preferentially occupies this site [86]. This result is in agreement with Moze and Buschow's study of the $YFe_{12-x}Cr_x$ system [112]. It id also in perfect agreement with the Rietveld refinement of the XRD patterns and with the fitting of the Mössbauer spectra of $GdFe_{12-x}Cr_x$ compounds.

Using first-principle calculations, Dirba et al. [113] determined the formation energy and magnetic moments for the three inequivalent sites 8*i*, 8*j* and 8*f* in the $SmFe_{11}M$, for various M elements. The formation energy was calculated as follow:

$$\Delta E = E[\mathrm{SmFe_{11}M}] - (E[\mathrm{SmFe_2}] + 9E[\mathrm{Fe}] + E[\mathrm{M}]).$$

They found that the substitution of Fe atoms by Ti, V, or Ga enhances the stability of the $I4/mmm$ $SmFe_{11}M$ compound (Figure 11), since the calculated formation energies for these elements was found lower than for Co, Cu atoms.

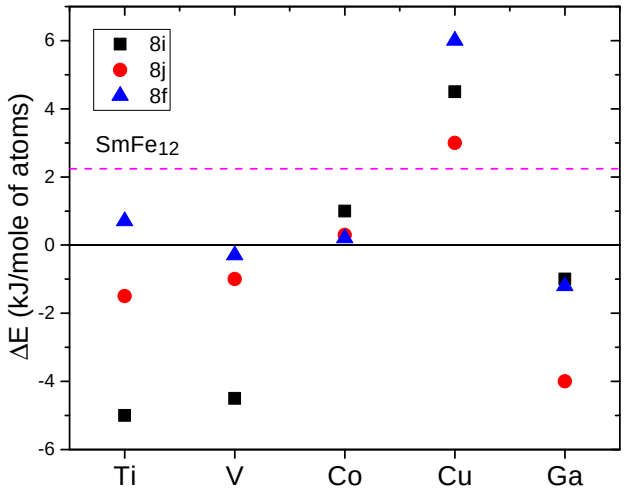

Figure 11. Calculated formation energy for $SmFe_{11}M$ (M = Ti, V, Co, Cu, Ga) [113]. The magenta dashed line corresponds to formation energy of the hypothetical $SmFe_{12}$ energy.

Using ab-initio calculations, Sikora et al. have determined the electronic structure for $Gd_{0.4}Tb_{0.6}Co_2$ intermetallic compound. They have found that cobalt's magnetic moments, estimated from X-ray photo-electron spectroscopy, are comparable with magnetic moment derived from DFT ab initio calculations [114]. In addition, they showed an anti-parallel alignment between R (R = Gd, Tb) and Co magnetic moments.

Moreover, we have compared the results of magnetic moments between those obtained by experimental measurements (Mössbauer Spectrometry) and those derived using theoretical ab initio DFT calculations for $YFe_{11}Ti$, $PrFe_{11}Ti$, and $GdFe_{10}Cr_2$ compounds. A good agreement have been obtained. These results are summarized in Table 10.

Table 9. Calculated energy E (Ry) of $GdFe_{10}Cr_2$, $YFe_{11}Cr$, $YFe_{11}Ti$, and $YFe_{11}V$ with Cr, Ti, and V atoms occupying different sites.

Compound	8*i*	8*j*	8*f*	Ref.
$GdFe_{10}Cr_2$	−104,440.2439	−104,440.2112	−104,440.2026	[86]
$YFe_{11}Cr$	−36,874.7094	−36,874.6956	−36,874.6966	[115]
$YFe_{11}Ti$	−36,480.6233	−36,480.6114	−36,480.6025	[84]
$YFe_{11}V$	−36,671.7028	−36,671.6735	−36,671.6745	[116]

Table 10. Comparison between magnetic moments, in μ_B/at., obtained by experimental measurements (Mössbauer Spectrometry) and by DFT calculations for $YFe_{11}Ti$, $PrFe_{11}Ti$, and $GdFe_{10}Cr_2$ [84,86].

	$\mu_{Fe}\{8i\}$	$\mu_{Fe}\{8i\}$	$\mu_{Fe}\{8i\}$	$\langle\mu_{Fe}\rangle$
$YFe_{11}Ti$				
Mössbauer	1.98	1.77	1.56	1.77
Calculated	2.49	2.07	1.88	1.90
$PrFe_{11}Ti$				
Mössbauer	2.00	1.84	1.69	1.82
Calculated	2.53	2.16	1.91	2.12
$GdFe_{10}Cr_2$				
Mössbauer	2.10	2.04	1.98	2.03
Calculated	2.46	2.36	2.12	2.28

5. Extrinsic Magnetic Properties

In this section, we will show the link between microstructure and extrinsic magnetic properties. Before presenting an example of our work on the study of $Sm(Fe,Si)_9$ car-

bides, we will summarize the most recent works that concern hard magnetic intermetallics prepared by HEBM.

Pal et al. [117] have found that $Nd_2Fe_{14}B$ alloy, obtained by HEBM, exhibits high coercivity at room temperature, more than 12 kOe. They concluded that HEBM synthesis method produces effective and less costly as compared to other methods reported earlier. Using HEBM Zhong et al. showed that for the optimized microstructure of $Nd_2(Fe,Co)_{14}B$ alloy the coercivity is about 10 kOe with a M_S equal to 75 emu/g [118]. Nanoflakes of $SmCo_5$ obtained by HEBM were mixed with Co nanowires in order to obtain $SmCo_5$/Co composites, the highest coercivity obtained is equal to 15 kOe [119]. These 3 examples demonstrate an important aspect: without modifying the structure and/or composition, the values for coercivity can be changed and optimized by adapting the synthesis method.

Through the example of $SmFe_{9-x}Si_xC$ carbides, we will see some synthesis parameters that influence the coercivity and explain the reason. The coercive fields measured at room temperature for the nanocrystalline carbide $SmFe_{9-x}Si_xC$ compounds ($x = 0.25, 1$) as a function of the annealing temperature T_A of the HEBM samples before carbonation, shown in Figure 12. For $T_A > 1000$ °C the hexagonal $P6/mmm$ structure turns into rhombohedral $R\bar{3}m$ one. At $T_A = 750$ °C, a maximum of coercive force of 15 kOe was obtained for $SmFe_{8.75}Si_{0.25}C$ compound, while for $SmFe_8Si_1C$, which is described by the space group $P6/mmm$, the maximum of H_C seems to move towards 800 °C. The value of H_C remains high, close to 13 kOe, for $x = 0.5$ but decreases towards 8.5 kOe for $x = 1$. This evolution can be linked to the variation of the crystallographic unit cell volume. Indeed the volume augmentation under the effect of carbonation decreases with the silicon content. The relative increase in volume $\Delta V/V$ varies from 3.70% for $x = 1$ to 5.05% for $x = 0.25$. This effect is, on the one hand, in agreement with the increase of the magnetic moment per iron atom, and on the other hand, it might correspond to a reduction of the magnetic anisotropy field with the increase of the silicon content.

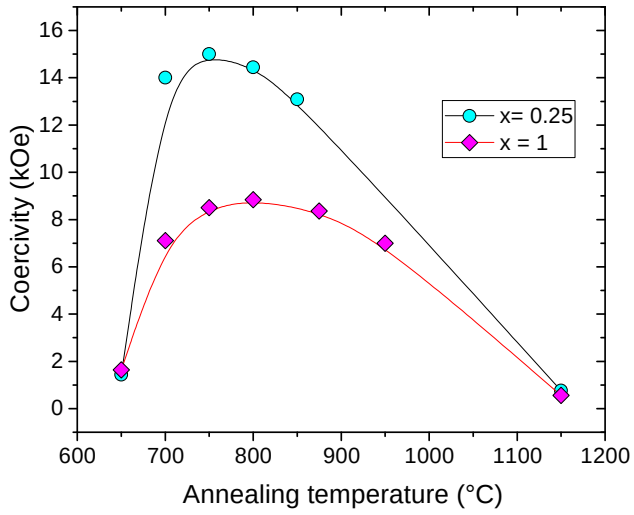

Figure 12. Room temperature coercivity vs annealing temperature for $SmFe_{9-x}Si_xC$.

The analysis of the coercivity suggests two different regimes depending on T_A. A too low annealing temperature slows down the reaction in the solid state leading to the metastable $Sm(Fe,Si)_9C$ phase responsible for the magnetic hardening. A higher annealing temperature reduces the number of defects in the $P6/mmm$ phase. This results in an increase of H_C, but on the other hand, the size of the diffraction domains increases which decreases H_C.

High-resolution transmission electron microscopy (HRTEM) was used to study the morphology of these specific samples (Figure 13). Measurements of inter-reticular distances from fringe system processing offer the possibility to identify grains from their crystallographic parameters. For the $SmFe_{8.75}Si_{0.25}C$ compound, annealed at $T_A = 650$ °C, the grain size is small around 10 nm and H_C is equal to 1.5 kOe. For the same sample annealed

at a higher temperature (1150 °C), the grain size is around 40 nm and the corresponding coercive field is equal to 0.8 kOe.

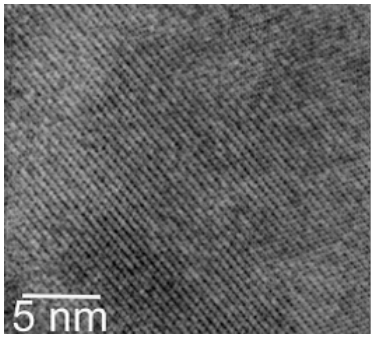

Figure 13. High-resolution Transmission Electron Microscopy (HRTEM) image for the best microstructure corresponding to domain size of 22 nm.

For the sample with the best coercive field, 15 kOe, the grain size is on the order of 22 nm in agreement with the Rietveld analysis. It appears that the grain boundaries connect neighboring grains without an inter-granular layer of measurable size, which favors the magnetic exchange coupling between grains. Moreover, a slight increase of the M_R/M_S ratio equal to 0.6 is observed (M_R represents the remanent magnetization and M_S the saturation magnetization). This could be explained by the exchange coupling between the grains of the main phase, rather than by the intermediary of the iron grains found in small quantities by crystallographic analysis and Mössbauer spectroscopy. Indeed the same tendency is observed for the M_R/M_S ratio, for the other compositions which do not contain free iron. The high coercivity of these compounds obtained by HEBM followed by annealing results from the non-equilibrium precursor phase $Sm(Fe,Si)_9C$ rather than from the equilibrium compounds $Sm_2(Fe,Si)_{17}C_2$.

In addition, nanocrystalline compounds $PrCo_3$, Pr_2Co_7 and Pr_5Co_{19}, constituted of intergrowths of AB_5-AB_2 stacking blocks, were studied [120–122]. Thanks to the optimization of their microstructures we obtained the following coercivities 12 kOe, 18 kOe, 15 kOe for $PrCo_3$, Pr_2Co_7, Pr_5Co_{19}, respectively. More recently, Bajorek et al. have shown a very significant potential for low-cost synthesis method of nanocrystalline hard magnetic $SmCo_5$ compound [48]. They used an innovative wet milling method that allowed them to optimize the microstructure for better extrinsic magnetic properties [43,45–48].

6. Conclusions

In this review, we have presented the structural and magnetic properties of some R-Fe-M-X intermetallics obtained by high energy milling. The combined effect of chemical substitution and light element insertion has been highlighted to optimize the intrinsic magnetic properties. The evolution of the Curie temperature is interpreted in terms of electronic effect and/or magnetovolume effect. The results of the magnetic measurements have been compared to the theoretical ab initio calculations and to the magnetic moments deduced from the hyperfine field measured by Mössbauer spectrometry. Finally, for the nanocrystalline hard magnetic materials, we showed the relationship between the extrinsic magnetic properties and the optimized microstructure of the nanocrystalline intermetallics.

Funding: This research received no external funding.

Institutional Review Board Statement: Not applicable.

Informed Consent Statement: Not applicable.

Data Availability Statement: Data available on request due to restrictions e.g., privacy or ethical.

Acknowledgments: The author thanks V. Charbonnier for her help.

Conflicts of Interest: The author declares no conflict of interest.

Abbreviations

The following abbreviations are used in this manuscript:

DFT	Density Functional Theory
δ	Isomer shift
HEBM	High-energy ball milling
HRTEM	High-resolution transmission electron microscopy
H_{HF}	Hyperfine field
H_C	Coercivity
M_R	Remanent magnetization
M_S	Saturation magnetization
R	Rare-earth
T_A	Annealing temperature
T_C	Curie temperature
WSC	Wigner-Seitz cell
XRD	X-ray Diffraction

References

1. Buschow, K.H.J. New developments in hard magnetic materials. *Rep. Prog. Phys.* **1991**, *54*, 1123. [CrossRef]
2. Burzo, E. Exchange Interactions and Transition Metal Moments in Rare-Earth Compounds. *J. Synchrotron Investig.* **2018**, *12*, 431–435. [CrossRef]
3. Zhang, Y. Review of the structural, magnetic and magnetocaloric properties in ternary rare earth RE_2T_2X type intermetallic compounds. *J. Alloys Compd.* **2019**, *787*, 1173–1186. [CrossRef]
4. Wang, Y.; Guo, D.; Wu, B.; Geng, S.; Zhang, Y. Magnetocaloric effect and refrigeration performance in $RE_{60}Co_{20}Ni_{20}$ (RE = Ho and Er) amorphous ribbons. *J. Magn. Magn. Mater.* **2020**, *498*, 166179. [CrossRef]
5. Li, L.; Yan, M. Recent progresses in exploring the rare earth based intermetallic compounds for cryogenic magnetic refrigeration. *J. Alloys Compd.* **2020**, *823*, 153810. [CrossRef]
6. Yin, L.; Parker, D.S. Effect of atom substitutions on the magnetic properties in Ce_2Fe_{17}: Toward permanent magnet applications. *J. Appl. Phys.* **2021**, *129*, 103902. [CrossRef]
7. Givord, D.; Lemaire, R. Magnetic Tranition and Anomalous Thermal-Expansion in R_2Fe_{17} Compounds. *IEEE Trans. Magn.* **1974**, *MAG-10*, 109. [CrossRef]
8. Coey, J.M.D.; Sun, H. Improved Magnetic Properties by Treatment of Iron-Based Rare-Earth Intermetallic Compounds in Ammonia. *J. Magn. Magn. Mater.* **1990**, *87*, L251–L254. [CrossRef]
9. Rodríguez-Carvajal, J.; Fernandez-Diaz, M.T.; Martinez, J.L. Neutron-Diffraction Study on Structural and Magnetic Properties of La_2NiO_4. *J. Phys. Condens. Matter* **1991**, *3*, 3215. [CrossRef]
10. Wang, Z.; Dunlap, R.A. Effects of Al Substitutions on the Magnetic Anisotropy of Sm_2Fe_{17} Compounds. *J. Phys. Condens. Matter* **1993**, *5*, 2407. [CrossRef]
11. Valeanu, M.; Plugaru, N.; Burzo, E. Effect of Nitrgenation on the Magnetic Properties of $Y_2Fe_{17-x}M_x$ Compounds, with M = Al, Ga or Si. *Solid State Commun.* **1994**, *89*, 519–522. [CrossRef]
12. Shen, B.G.; Liang, B.; Wang, F.W.; Cheng, Z.H.; Gong, H.Y.; Zhang, S.Y.; Zhang, J.X. Magnetic Properties of $Sm_2Fe_{17-x}Si_x$ and $Sm_2Fe_{17-x}Si_xC$ Compounds. *J. Appl. Phys.* **1995**, *77*, 2637. [CrossRef]
13. Shen, B.G.; Cheng, Z.H.; Liang, B.; Guo, H.Q.; Zhang, J.X.; Gong, H.Y.; Wang, F.W.; Yan, Q.W.; Zhan, W.S. Structure and Magnetocrystalline Anisotropy of $R_2Fe_{17-x}Ga_x$ Compounds with Higher Ga Concentration. *Appl. Phys. Lett.* **1995**, *67*, 1621. [CrossRef]
14. Middleton, D.P.; Mishra, S.R.; Long, G.J.; Pringle, O.A.; Hu, Z.; Yelon, W.B.; Grandjean, F.; Buschow, K.H.J. Magnetic, Neutron Diffraction, and Mossbauer Spectral Study of the $Ce_2Fe_{17-x}Si_x$ Solid Solutions. *J. Appl. Phys.* **1995**, *78*, 5568–5576. [CrossRef]
15. Sabirianov, R.F.; Jaswal, S.S. Electronic structure and magnetism in $Sm_2Fe_{17-x}A_x$ (A=Al,Ga,Si). *J. Appl. Phys.* **1996**, *79*, 5942. [CrossRef]
16. Yelon, W.B.; Hu, Z.; James, W.J.; Marasinghe, G.K. Site affinity of substituents in $Nd_2Fe_{17?x}T_x$ (T=Cu,Zr,Nb,Ti,V) alloys. *J. Appl. Phys.* **1996**, *79*, 5939. [CrossRef]
17. Koch, E.; Fischer, W. DIDO95 and VOID95 - Programs for the calculation of Dirichlet domains and coordination polyhedra. *Z. Kristallogr.* **1996**, *211*, 251. [CrossRef]
18. Dunlap, R.A.; MacKay, G.R.; Wang, Z. A Mossbauer effect investigation of site preferences and Fe environments in Ga-substituted Sm_2Fe_{17} compounds. *J. Alloys Compd.* **1997**, *260*, 28–31. [CrossRef]
19. Girt, E.; Altounian, Z.; Yang, J. Structural and magnetic properties of $Nd_2Fe_{17-\delta}Cr_\delta$ ($\delta = 0, 0.5, 1, 1.9$). *J. Appl. Phys.* **1997**, *8*, 5118. [CrossRef]
20. Burzo, E. Permanent magnets based on R-Fe-B and R-Fe-C alloys. *Rep. Prog. Phys.* **1998**, *61*, 1099. [CrossRef]
21. Forker, M.; Julius, A.; Shulte, M.; Best, D. Mossbauer study of the hyperfine interaction of Fe-57 in $Y_{1-s}Co_{5+2s}$ and related compounds. *Phys. Rev. B* **1998**, *57*, 11565. [CrossRef]

22. Givord, D.; Courtois, D. Exchange interactions in R-M intermetallics. *J. Magn. Magn. Mater.* **1999**, *196*, 684. [CrossRef]
23. Djega-Mariadassou, C.; Bessais, L. Emergence of order in nanocrystalline $SmFe_9$. *J. Magn. Magn. Mater.* **2000**, *210*, 81. [CrossRef]
24. Teresiak, A.; Kubis, M.; Mattern, N.; Müller, K.H.; Wolf, B. Crystal structure of $Sm_2Fe_{17-y}M_y$ compounds with M = Al, Si, Ga. *J. Alloys Compd.* **2001**, *319*, 168. [CrossRef]
25. Bessais, L.; Djega-Mariadassou, C. Structure and magnetic properties of nanocrystalline $Sm(Fe_{1-x}Co_x)_{11}Ti$ ($x \leq 2$). *Phys. Rev. B* **2001**, *63*, 54412. [CrossRef]
26. Bessais, L.; Djega-Mariadassou, C.; Koch, E. Structural and Mossbauer spectral study of the metastable phase $Sm(Fe, Co, Ti)_{10}$. *J. Phys. Condens. Matter* **2002**, *14*, 8111. [CrossRef]
27. Bessais, L.; Djega-Mariadassou, C.; Nandra, A.; Appay, M.D.; Burzo, E. Hard magnetic $Sm(Fe,Si)_9$ carbides: Structured and magnetic properties. *Phys. Rev. B* **2004**, *69*, 64402. [CrossRef]
28. Bessais, L.; Djega-Mariadassou, C.; Tung, D.K.; Hong, V.V.; Phuc, N.X. A ^{57}Fe Mossbauer study of nanostructured $Sm_2Fe_{17-x}Co_xC_3$. *J. Alloys Compd.* **2008**, *455*, 35. [CrossRef]
29. Khazzan, S.; Mliki, N.; Bessais, L. Structure and magnetic properties of nanocrystalline $Sm_{1-s}(Fe,Mo)_{5+2s}$. *J. Appl. Phys.* **2009**, *105*, 103904. [CrossRef]
30. Khazzan, S.; Mliki, N.; Bessais, L.; Djega-Mariadassou, C. Rare-earth iron-based intermetallic compounds and their carbides: Structure and magnetic behaviors. *J. Magn. Magn. Mater.* **2010**, *322*, 224–229. [CrossRef]
31. Galler, A.; Ener, S.; Maccari, F.; Dirba, I.; Skokov, K.P.; Gutfleisch, O.; Biermann, S.; Pourovskii, L.V. Intrinsically weak magnetic anisotropy of cerium in potential hard-magnetic intermetallics. *NPJ Quantum Mater.* **2021**, *2*, 6. [CrossRef]
32. Opelt, K.; Ahmad, T.; Diehl, O.; Schonfeldt, M.; Brouwer, E.; Vogel, I.; Rossa, J.D.; Gassmann, J.; Ener, S.; Gutfleisch, O. Upscaling the 2-Powder Method for the Manufacturing of Heavy Rare-Earth-Lean Sintered didymium-Based Magnets. *Adv. Eng. Mater.* **2021**, *23*, 2100459. [CrossRef]
33. Dirba, I.; Sepehri-Amin, H.; Skokov, K.; Skourski, Y.; Hono, K.; Gutfleisch, O. Magnetic properties and microstructure of Sm_5Fe_{17}-based composite magnets. *Acta Mater.* **2021**, *212*, 116912. [CrossRef]
34. Hosokawa, A.; Suzuki, K.; Yamaguchi, W.; Takagi, K. Mechanism of anomalous α-Fe formation from stoichiometric Sm_2Fe_{17} jet-milled powder during post-pulverization annealing. *Acta Mater.* **2021**, *213*, 116981. [CrossRef]
35. Ener, S.; Skokov, K.P.; Palanisamy, D.; Devillers, T.; Fischbacher, J.; Eslava, G.G.; Maccari, F.; Schafer, L.; Diop, L.V.B.; Radulov, I.; et al. Twins—A weak link in the magnetic hardening of $ThMn_{12}$-type permanent magnets. *Acta Mater.* **2021**, *214*, 116968. [CrossRef]
36. Schafer, L.; Skokov, K.; Liu, J.; Maccari, F.; Braun, T.; Riegg, S.; Radulov, I.; Gassmann, J.; Merschroth, H.; Harbig, J.; et al. Design and Qualification of Pr-Fe-Cu-B Alloys for the Additive Manufacturing of Permanent Magnets. *Adv. Funct. Mater.* **2021**, *31*, 2102148. [CrossRef]
37. Coey, J.M.D. Novel Permanent Magnetic Materials. *Phys. Scr.* **1991**, *T39*, 21–28. [CrossRef]
38. Coey, J.M.D. Perspective and Prospects for Rare Earth Permanent Magnets. *Engineering* **2020**, *6*, 119–131. [CrossRef]
39. Kovacs, A.; Fischbacher, J.; Gusenbauer, M.; Oezelt, H.; Herper, H.C.; Vekilova, O.Y.; Nieves, P.; Arapan, S.; Schrefl, T. Computational Design of Rare-Earth Reduced Permanent Magnets. *Engineering* **2020**, *6*, 148–153. [CrossRef]
40. Onoue, M.; Kobayashi, R.; Mitsui, Y.; Umetsu, R.Y.; Uwatoko, Y.; Koyama, K. Magnetic field-induced nitridation of Sm_2Fe_{17}. *J. Alloys Compd.* **2020**, *835*, 155193. [CrossRef]
41. Liu, K.; Wang, S.H.; Feng, Y.L.; Zhang, Y.K. Research on Phases and Morphology of Sm_2Fe_{17} Melt-Spun Ribbon. *Rare Met. Mat. Eng.* **2020**, *49*, 3796–3802.
42. Dahal, J.N.; Ali, K.S.S.; Mishra, S.R.; Neupane, D. Effect of Ga and Zr Substitution on the Properties of $Dy_2Fe_{17-x}Zr_x$ and $Dy_2Fe_{16}Ga_{1-x}Zr_x$ ($0 \leq x \leq 1$) Intermetallic Compounds Prepared via Arc Melting Process. *Magnetochemistry* **2020**, *6*, 9. [CrossRef]
43. Chrobak, A.; Bajorek, A.; Chełkowska, G.; Haneczok, G.; Kwiencien, M. Magnetic properties and magnetocaloric effect of the $Gd(Ni_{1-x}Fe_x)_3$ crystalline compound and powder. *Phys. Stat. Sol.* **2009**, *206*, 731–737.
44. Phejar, M.; Paul-Boncour, V.; Bessais, L. Investigation on structural and magnetocaloric properties of $LaFe_{13-x}Si_x(H,C)_y$ compounds. *J. Solid State Chem.* **2016**, *233*, 95–102. [CrossRef]
45. Bajorek, A.; Berger, C.; Pruzik, K.; Zubko, M.K.; Wojtyniak, M.; Chełkowska, G. Novel $Ho(Ni_{0.8}Co_{0.2})_3$ nanoflakes produced by high energy ball-milling. *Mater. Charcterisation* **2017**, *128*, 45–53.
46. Łopadczak, P.; Bajorek, A.; Prusik, K.; Zubko, M.; Chełkowska, G. Magnetic hardening induced in RCo_5 (R = Y, Gd, Sm) by short HEBM. *Acta Phyica Pol. A* **2018**, *55*, 2100904.
47. Bajorek, A.; Łopadczak, P.; Prusik, K.; Zubko, M.; Chełkowska, G. The comparison of magnetic properties at room temperature in RCo_5 (R = Y, Sm, Gd) nanoflakes synthesized via time-staged HEBM. *IEEE Trans. Magn.* **2019**, *55*, 2100904.
48. Bajorek, A.; Łopadczak, P.; Prusik, K.; Zubko, M. Correlation between Microstructure and Magnetism in Ball-Milled $SmCo_5/\alpha$-Fe (5%wt. α-Fe) Nanocomposite Magnets. *Materials* **2021**, *14*, 502. [CrossRef] [PubMed]
49. Veselova, S.; Tereshina, I.; Verbetsky, V.; Neznakhin, D.; Tereshina-Chitrova, E.; Kaminskaya, T.; Karpenkov, A.; Akimova, O.; Gorbunov, D.; Savchenko, A. Structure and magnetic properties of $(Sm,Ho)_2Fe_{17}N_x$ (x = 0; 2.4). *J. Magn. Magn. Mater.* **2020**, *502*, 166549. [CrossRef]
50. Shen, B.G.; Wang, F.W.; Gong, H.Y.; Cheng, Z.H.; Liang, B.; Zhang, J.X.; Zhang, S.Y. Magnetic properties of $Sm_2Fe_{17-x}Ga_xC_2$ compounds. *J. Phys. Condens. Matter* **1995**, *7*, 883. [CrossRef]

51. van Lier, J.; Kubis, M.; Grünberger, W.; Shultz, L.; Kronmüller, H. High performance $Sm_{2+\delta}Fe_{15}Ga_2C_2$ permanent magnets made by melt spinning and hot pressing. *J. Appl. Phys.* **1998**, *83*, 5549. [CrossRef]
52. Kubis, M.; Eckert, D.; Gebel, B.; Müller, K.H.; Schultz, L. Intrinsic magnetic properties of $Sm_2Fe_{17-x}M_xN_y/C_y$ (M= Al, Ga or Si). *J. Magn. Magn. Mater.* **2000**, *217*, 14. [CrossRef]
53. Cao, L.; Handstein, A.; Gebel, B.; Schäfer, R.; Müller, K.H. Thermostability of $Sm_2(FeGa)_{17}C_y$ prepared by gas-solid reaction (GSR). *J. Appl. Phys.* **1997**, *81*, 4539. [CrossRef]
54. Schultz, L.; Schnitzke, K.; Wecker, J.; Katter, M.; Kuhrt, C. Permanent magnets by mechanical alloying. *J. Appl. Phys.* **1991**, *70*, 6339. [CrossRef]
55. Christodoulou, C.N.; Takeshita, T. Preparation, structural and magnetic properties and stability of interstitial Sm_2Fe_{17}-carbonitrohydrides. *J. Alloys Compd.* **1993**, *198*, 1–24. [CrossRef]
56. Mao, O.; Altounian, Z.; Yang, J.; Strom-Olsen, O. Thermal stability of nanostructured $Sm_2Fe_{17}C_x$ compounds prepared by ball milling. *J. Appl. Phys.* **1996**, *79*, 5536. [CrossRef]
57. Fersi, R.; Cabie, M.; Mliki, N.; Bessais, L. Impact of carbon insertion on the microstructure and magnetic properties of nanocrystalline Pr_2Co_7 alloys. *J. Alloys Compd.* **2013**, *576*, 415–423. [CrossRef]
58. Bouzidi, W.; Mliki, N.; Bessais, L. Effect of carbonation on the structural, magnetic and magnetocaloric properties of uniaxial nanocrystalline $Pr_5Co_{19}C_x$ compound. *J. Magn. Magn. Mater.* **2018**, *466*, 411–419. [CrossRef]
59. Yamkane, Z.; Fersi, R.; Rachid, F.Z.; Moubah, R.; Lassri, H.; Mliki, N.; Alleg, S.; Sajieddine, M.; Bessais, L. Law of approach to magnetic saturation in nanocrystalline $Pr_2Co_7C_x$ ($x \leq 1$): Effects of carbonation. *SPIN* **2020**, *10*, 2050016. [CrossRef]
60. Buschow, K.H.J.; Goot, A.S.V.D. Intermetallic compounds in the system samarium-cobalt. *J. Less-Common. Met.* **1968**, *14*, 323. [CrossRef]
61. Givord, D.; Laforest, J.; Scweizer, J.; Tasset, F. Temperature dependence of the samarium magnetic form factor in $SmCo_5$. *J. Appl. Phys.* **1979**, *50*, 2008. [CrossRef]
62. Bartoli, T.; Joubert, J.M.; Provost, K.; Elkaim, E.; Paul-Boncour, V.; Monnier, J.; Moscovici, J.; Bessais, L. Site Occupancy Determination in Th_2Zn_{17}- and $TbCu_7$-types $Sm_2Fe_{17-x}Co_x$ Compounds using Synchrotron Resonant Diffraction. *Inorg. Chem.* **2021**, *60*, 1533–1541. [CrossRef] [PubMed]
63. Shield, J.; Meacham, B.E. Phase formation in hypostoichiometric Sm_2Fe_{17} alloys modified with Ti and C. *J. Appl. Phys.* **2000**, *87*, 2055. [CrossRef]
64. Meacham, B.E.; Shieldm, J.; Branagan, D. Order-disorder effects in nitrided Sm-Fe permanent magnets. *J. Appl. Phys.* **2000**, *87*, 6707. [CrossRef]
65. Zheng, C.; Yu, D.; Li, K.; Luo, Y.; Jin, J.; Lu, S.; Li, H.; Mao, Y.; Quan, N. Effect of boron additions on phase formation and magnetic properties of TbCu7-type melt spun SmFe ribbons. *J. Magn. Magn. Mater.* **2016**, *412*, 89–94. [CrossRef]
66. Yang, W.; Zha, L.; Lai, Y.; Qiao, G.; Du, H.; Liu, S.; Wang, C.; Han, J.; Yang, Y.; Hou, Y.; et al. Structural and magnetic properties of the $R_{10}Fe_{90-x}Si_x$ alloys with R=Y, Ce,Pr, Nd, Sm, Gd, Tb, Dy, Ho, and Er. *Intermetallics* **2018**, *90*, 8–17. [CrossRef]
67. Saito, T.; Miyoshi, H.; Nishio-Hamane, D. Magnetic properties of Sm-Fe-Ti nanocomposite magnets with a $ThMn_{12}$ structure. *J. Alloys Compd.* **2012**, *519*, 144–148. [CrossRef]
68. Luo, Y.; Zhang, K.; Li, K.S.; Yu, D.B.; Ling, J.J.; Men, K.; Dou, Q.Y.; Yan, W.L.; Xie, J.J.; Yang, Y.F. Structure and magnetic behaviors of melt-spun SmFeSiB ribbons and their nitrides. *J. Magn. Magn. Mater.* **2018**, *405*, 214–218. [CrossRef]
69. Takagi, K.; Jinno, M.; Ozaki, K. Preparation of $TbCu_7$-type Sm-Fe powders by low-temperature HDDR treatment. *J. Magn. Magn. Mater.* **2018**, *454*, 170–175. [CrossRef]
70. Wu, G.; Li, H.; Yu, D.; Li, K.; Yan, W.; Yuan, C.; Sun, L.; Luo, Y.; Zhang, K. Effect of niobium substitution on microstructures and thermalstability of $TbCu_7$-type Sm-Fe-N magnets. *J. Rare Earths* **2018**, *36*, 281–286. [CrossRef]
71. Yan, W.; Quan, N.; Luo, Y.; Yu, D.; Wang, Z.; Wu, G.; Zhang, K. Structure and hard magnetic properties of TbCu7-type $SmFe_{8.95-x}Ga_{0.26}Nb_x$ nitrides. *J. Rare Earths* **2018**, *36*, 165–169. [CrossRef]
72. Saito, T.; Watanabe, F.; Nishio-Hamane, D. Magnetic properties of $SmFe_{12}$-based magnets produced by sparkplasma sintering method. *J. Alloys Compd.* **2019**, *773*, 1018–1022. [CrossRef]
73. de Mooij, D.B.; Buschow, K.H.J. Some novel ternary $ThMn_{12}$-type compounds. *J. Less-Common. Met.* **1988**, *136*, 207. [CrossRef]
74. Teatum, E.T.; Gschneidner, K.A.; Waber, J.T. *Rep. LA-4003*; Los Alamos Scientific Lab: Los Alamos, NM, USA, 1968.
75. Nehdi, I.; Bessais, L.; Djega-Mariadassou, C.; Abdellaoui, M.; Zarrouk, H. X-ray and Mössbauer studies of $Sm_2Fe_{17-x}Cr_x$ materials synthesized by 2 172x xmechanical alloying followed by an appropriate short annealing. *J. Alloys Compd.* **2003**, *351*, 24–30. [CrossRef]
76. Schramm, L.; Acker, J.; Wetzig, K. Structural effects of Zr substitution in the 1:7- and 2:17-type structure. *J. Alloys Compd.* **2006**, *414*, 158–168. [CrossRef]
77. Cadieu, F.J.; Hegde, H.; Navarathna, A.; Rani, R.; Chen, K. High-energy product $ThMn_{12}$ Sm-Fe-T and Sm-Fe permanent magnets synthesized as oriented sputtered films. *Appl. Phys. Lett.* **1991**, *59*, 875. [CrossRef]
78. Wang, D.; Liou, S.; He, P.; Sellmyer, D.; Hadjipanayis, G.; Zhang, Y. $SmFe_{12}$ and $SmFe_{12}N_x$ films fabricated by sputtering. *J. Magn. Magn. Mater.* **1993**, *124*, 62. [CrossRef]
79. Verhoef, R.; de Boer, F.; Zhi-dong, Z.; Buschow, K.H.J. Moment reduction in $RFe_{12-x}T_x$ compounds (R=Gd, Y and T=Ti, Cr, V, Mo, W). *J. Magn. Magn. Mater.* **1988**, *75*, 319. [CrossRef]

80. Buschow, K.H.J. Permanent magnet materials based on tetragonal rare earth compounds of the type $RFe_{12-x}M_x$. *J. Magn. Magn. Mater.* **1991**, *100*, 79. [CrossRef]
81. Cizmas, C.B.; Djega-Mariadassou, C.; Bessais, L. Effect of Si content on magnetic properties and intersublattice exchange interactions in $GdFe_{11-x}Si_xTi$ compounds. *J. Magn. Magn. Mater.* **2001**, *226–230*, 1171–1173. [CrossRef]
82. Bessais, L.; Sab, S.; Djega-Mariadassou, C.; Greneche, J.M. Crystallographic and hyperfine parameters of $PrTi(Fe,Co)_{11}$ and their carbides. *Phys. Rev. B* **2002**, *66*, 054430. [CrossRef]
83. Bouzidi, W.; Bartoli, T.; Sedek, R.; Bouzidi, A.; Moscovici, J.; Bessais, L. Low Field Magnetocaloric Effect of $NdFe_{11}Ti$ and $SmFe_{10}V_2$ Compounds. *J. Mater. Sci. Mater. Electron.* **2021**, *32*, 10579–10586. [CrossRef]
84. Bouhbou, M.; Moubah, R.; Hlil, E.; Lassri, H.; Bessais, L. Electronic structure, hyperfine parameters and magnetic properties of $RFe_{11}Ti$ intermetallic compounds (R = Y, Pr): Ab initio calculations, SQUIDmagnetometry and Mössbauer studies. *J. Magn. Magn. Mater.* **2021**, *518*, 167362. [CrossRef]
85. Khazzan, S.; Bessais, L.; Tendeloo, G.V.; Mliki, N. Correlation of nanocrystalline $Sm(Fe,Mo)_{12}$ and its out of equilibrium phase $Sm(Fe,Mo)_{10}$. *J. Magn. Magn. Mater.* **2014**, *363*, 125–132. [CrossRef]
86. Saidi, M.; Walha, S.; Hlil, E.; Bessais, L.; Jemmali, M. Effect of chromium substitution on structural, magnetic and magnetocaloric properties of $GdFe_{12-x}Cr_x$ intermetallic compounds, Mössbauerspectrometry and ab initio calculations. *J. Solid State Chem.* **2021**, *297*, 122019. [CrossRef]
87. de Boer, F.R.; Huang, Y.K.; de Mooij, D.B.; Buschow, K.H.J. Magnetic properties of a series of novel ternary intermetallics ($RFe_{10}V_2$). *J. Less-Common. Met.* **1987**, *135*, 139. [CrossRef]
88. Nan-xian, C.; Shi-qiang, H.; Yu, W.; Jiang, S. Phase stability and site preference of $Sm(Fe,T)_{12}$. *J. Magn. Magn. Mater.* **2001**, *233*, 169–180. [CrossRef]
89. Buschow, K.H.J. Structure and properties of some novel ternary Fe-rich rare-earth intermetallics. *J. Appl. Phys.* **1988**, *63*, 3130–3135. [CrossRef]
90. Tang, S.L.; Yang, C.P.; Wang, B.W.; Jin, X.M.; Zhang, S.Y.; Du, Y.W. Structure and magnetic properties of $PrFe_{11.5-x}V_xTi_{0.5}$ compounds and their nitrides. *J. Magn. Magn. Mater.* **1998**, *189*, 341–345. [CrossRef]
91. Tang, S.L.; Yin, J.H.; Jin, Z.Q.; Zhang, J.R.; Zhang, S.Y.; Du, Y.W. Structure and magnetic properties of $PrFe_{10}V_xMo_{2-x}$ compounds and their nitrides. *J. Appl. Phys.* **1999**, *85*, 4687–4689. [CrossRef]
92. Tomey, E.; Bacmann, M.; Fruchart, D.; Soubeyroux, J.L.; Gignoux, D. Influence of hydrogen on the structural and magnetic properties of the $RFe_{10.5}Mo_{1.5}$ compounds (R=rare earth). *J. Alloys Compd.* **1995**, *231*, 195–200. [CrossRef]
93. Cizmas, C.B.; Djega-Mariadassou, C.; Bessais, L. Magnetic properties of $GdFe_{11-x}SixTi$. *J. Alloys Compd.* **2002**, *345*, 27–35. [CrossRef]
94. Li, Z.W.; Morrish, A.H. Negative exchange interactions and Curie temperatures for Sm_2Fe_{17-x} and $Sm_2Fe_{17-x}N_y$. *Phys. Rev. B* **1997**, *55*, 3670. [CrossRef]
95. Burzo, E.; Laforest, J.; Plugaru, N.; Valeanu, M.; Stanciu, L. Magnetic properties of $Gd_2Fe_{14-x}M_x$ compounds with M= Ni, Si, Cu or V. *IEEE Trans. Magn.* **1994**, *30*, 625. [CrossRef]
96. Djega-Mariadassou, C.; Bessais, L.; Nandra, A.; Grenèche, J.M.; Burzo, E. Structure and hyperfine properties of $Sm_2(Fe,Si)_{17}$. *Phys. Rev. B* **2001**, *65*, 14419. [CrossRef]
97. Bessais, L.; Dorolti, E.; Djega-Mariadassou, C. Correlation between $Sm_2(Fe,Ga)_{17}$ and its precursor $Sm(Fe,Ga)_9$. *J. Appl. Phys.* **2005**, *87*, 013902. [CrossRef]
98. Bessais, L.; Younsi, K.; Khazzan, S.; Mliki, N. X-ray and intrinsic magnetic properties of nanocrystalline $Sm_2(Fe,M)_{17}$ (M = Si,Ga, Co, Cr, Zr or Mo). *Intermetallics* **2011**, *19*, 997–1004. [CrossRef]
99. Hu, B.P.; Li, H.S.; Sun, H.; Coey, J.M.D. A ^{57}Fe Mossbauer study of a new series of rare-earth iron nitrides: $R_2Fe_{17}N_{3-\delta}$. *J. Phys. Condens. Matter* **1991**, *3*, 3983–3995. [CrossRef]
100. Bouchaala, N.; Jemmali, M.; Bartoli, T.; Nouri, K.; Hentech, I.; Walha, S.; Bessais, L.; Salah, A.B. Influence of Fe-substitution on structural, magnetic and magnetocaloric properties of $Nd_2Fe_{17-x}Co_x$ solid solutions. *J. Solid State Chem.* **2018**, *258*, 501–509. [CrossRef]
101. Saidi, M.; Nouri, K.; Walha, S.; Dhahri, E.; Kabadou, A.; Jemmali, M.; Bessais, L. Structural, Magnetic, Magnetocaloric and Mossbauer Spectrometry Study of $Gd_2Fe_{17-x}Cu_x$ ($x = 0, 0.5, 1$ and 1.5) Compounds. *J. Electron. Mater.* **2019**, *48*, 2242–2253. [CrossRef]
102. Charfeddine, S.; Zehani, K.; Bessais, L.; Korchef, A. Structural, magnetic, magneto-caloric and Mössbauer spectral study of Tb_2Fe_{17} compound synthesized by arc melting. *J. Solid State Chem.* **2016**, *238*, 15–20. [CrossRef]
103. Grandjean, F.; Isnard, O.; Long, G.J. Magnetic and Mossbauer spectral evidence for the suppression of the magnetic spin reorientationin Tm_2Fe_{17} by deuterium. *Phys. Rev. B* **2002**, *65*, 064429. [CrossRef]
104. Grandjean, F.; Isnard, O.; Hautot, D.; Long, G.J. Structural, magnetic, and Mossbauer spectral study of Er_2Fe_{17} and its hydrides. *Phys. Rev. B* **2000**, *63*, 014406. [CrossRef]
105. Sanchez, H.M.; Salazar, D.; Zamora, L.E.; Hernandez, J.S.T.; Tabares, J.A.; Alcazar, G.A.P. Mössbauer spectroscopy in the system $(Nd_{1-x}Ce_x)_{1.1}Fe_{10}CoTi$ with $ThMn_{12}$ structure. *Hyperfine Interact.* **2020**, *241*, 44. [CrossRef]
106. Gjoka, M.; Psycharis, V.; Devlin, E.; Niarchos, D.; Hadjipanayis, G. Effect of Zr substitution on the structural and magnetic properties of the series $Nd_{1-x}Zr_xFe_{10}Si_2$ with the ThMn12 type structure. *J. Alloys Compd.* **2016**, *687*, 240–245. [CrossRef]

107. Aubert, A.; Madugundo, R.; Schönhöbel, A.M.; Salazar, D.; Garitaonandia, J.S.; Barandiaran, J.M.; Hadjipanayis, G. Structural and magnetic properties of Nd-Fe-Mo-(N) melt-spun ribbons with $ThMn_{12}$ structure. *Acta Mater.* **2020**, *195*, 519–526. [CrossRef]
108. Harashima, Y.; Terakura, K.; Kino, H.; Ishibashi, S.; Miyake, T. First-principles study on stability and magnetism of $NdFe_{11}M$ and $NdFe_{11}MN$ for M = Ti, V, Cr, Mn, Fe, Co, Ni, Cu, Zn. *J. Appl. Phys.* **2016**, *120*, 203904. [CrossRef]
109. Harashima, Y.; Fukazawa, T.; Kino, H.; Miyake, T. Effect of *R*-site substitution and the pressure on stability of RFe_{12}: A first-principles study. *J. Appl. Phys.* **2018**, *124*, 163902. [CrossRef]
110. Yamashita, S.; Suzuki, D.; Yoshioka, T.; Tsuchiura, H.; Novak, P. Finite-temperature magnetic properties of $Sm_2Fe_{17}N_x$ using an ab initio effective spin model. *Phys. Rev. B* **2020**, *102*, 214439. [CrossRef]
111. Ogura, M.; Mashiyama, A.; Akai, H. Role of N in the Permanent Magnet Material $Sm_2Fe_{17}N_x$. *J. Phys. Soc. Jpn.* **2015**, *84*, 084702. [CrossRef]
112. Moze, O.; Buschow, K.H.J. Magnetic structure and preferred site occupation of Cr in the compound $YFe_{10}Cr_2$. *J. Alloys Compd.* **1996**, *233*, 165. [CrossRef]
113. Dirba, I.; Harashima, Y.; Sepehri-Amin, H.; Ohkubo, T.; Miyake, T.; Hirosawa, S.; Hono, K. Thermal decomposition of $ThMn_{12}$-type phase and its optimum stabilizing elements in $SmFe_{12}$-based alloys. *J. Alloys Compd.* **2020**, *813*, 152224. [CrossRef]
114. Sikora, M.; Bajorek, A.; Chrobak, A.; Deniszczyk, J.; Ziółkowski, G.; Chełkowska, G. Magnetic Properties and the Electronic Structure of the $Gd_{0.4}Tb_{0.6}Co_2$ Compound. *Materials* **2020**, *13*, 5481. [CrossRef]
115. Ma, H.F.; Huang, Z.; Chen, B.; Qiang, W.R.; Pan, M. The stabilization effect of substituted atoms and magnetism for intermetallic compounds $YFe_{12-x}Cr_x$. *Chin. Phys. B* **2009**, *18*, 1991–2005.
116. Ma, H.F.; Huang, Z.; Chen, B.; Qiang, W.R.; Sun, G.A. The stabilization effect of the substituted atoms and the magnetism for intermetallic compounds $YFe_{12-x}V_x$. *Sci. China* **2010**, *53*, 1239–1243.
117. Pal, A.; Gabay, A.; Hadjipanayis, G.C. Mechanochemical synthesis of $Nd_2Fe_{14}B$ alloy with high coercivity. *J. Alloys Compd.* **2012**, *543*, 31–33. [CrossRef]
118. Zhong, Y.; Chaudhary, V.; Tan, X.; Parmar, H.; Ramanujan, R. Kinetic study of the mechanochemical synthesis of $Nd_2(Fe,Co)_{14}B$ hardmagnetic nanoparticles. *J. Alloys Compd.* **2018**, *747*, 755–763. [CrossRef]
119. Zhu, K.; Xu, J.; Wang, X.; Li, W.; Tian, K.; Hou, Y. Chemical synthesis and coercivity enhancement of $Nd_2Fe_{14}B$ nanostructures mediated by non-magnetic layer. *Nano Res.* **2020**, *13*, 1141–1148. [CrossRef]
120. Younsi, K.; Russier, V.; Bessais, L. Structure and magnetic properties of nanocrystalline $PrCo_3$. *J. Appl. Phys.* **2010**, *107*, 083916. [CrossRef]
121. Fersi, R.; Mliki, N.; Bessais, L.; Guetari, R.; Russier, V.; Cabié, M. Effect of annealing on structural and magnetic properties of Pr_2Co_7 compounds. *J. Alloys Compd.* **2012**, *522*, 14–18. [CrossRef]
122. Bouzidi, W.; Mliki, N.; Bessais, L. Structural and magnetic properties of new uniaxial nanocrystallinePr5Co19 compound. *J. Magn. Magn. Mater.* **2017**, *441*, 566–571. [CrossRef]